

The Force Balance of Electrons During Kinetic Anti-parallel Magnetic Reconnection

J. Egedal,¹ H. Gurram,¹ S. Greess,¹ W. Daughton,² and A. Lê²

¹*Department of Physics, University of Wisconsin-Madison, Madison, Wisconsin 53706, USA*

²*Los Alamos National Laboratory, Los Alamos, New Mexico 87545, USA*

(*Electronic mail: egedal@wisc.edu)

(Dated: 6 April 2023)

Fully kinetic simulations are applied to the study of 2D anti-parallel reconnection, elucidating the dynamics by which the electron fluid maintains force balance within both the ion diffusion region (IDR) and the electron diffusion region (EDR). Inside the IDR, magnetic field-aligned electron pressure anisotropy ($p_{e\parallel} \gg p_{e\perp}$) develops upstream of the EDR. Compared to previous investigations, the use of modern computer facilities allows for simulations at the natural proton to electron mass ratio $m_i/m_e = 1836$. In this high- m_i/m_e -limit the electron dynamics changes qualitatively, as the electron inflow to the EDR is enhanced and mainly driven by the anisotropic pressure. Using a coordinate system with the x -direction aligned with the reconnecting magnetic field and the y -direction aligned with the central current layer, it is well-known that for the much studied 2D laminar anti-parallel and symmetric scenario the reconnection electric field at the X -line must be balanced by the $\partial p_{exy}/\partial x$ and $\partial p_{eyz}/\partial z$ off-diagonal electron pressure stress components. We find that the electron anisotropy upstream of the EDR imposes large values of $\partial p_{exy}/\partial x$ within the EDR, and along the direction of the reconnection X -line this stress cancels with the stress of a previously determined theoretical form for $\partial p_{eyz}/\partial z$. The electron frozen-in law is instead broken by pressure tensor gradients related to the direct heating of the electrons by the reconnection electric field. The reconnection rate is free to adjust to the value imposed externally by the plasma dynamics at larger scales.

I. INTRODUCTION

Magnetic reconnection¹ is the process that permits the magnetic topology of an electrically conducting plasma to rearrange, often accompanied by large scale release of stored magnetic energy. Well-known instances of reconnection occur in association with solar flares² and magnetic storms in the Earth's magnetosphere³. In resistive MHD models, reconnection is a slow diffusive process within narrow current layers⁴. In low collisional plasma, however, additional physical effects become important as the theoretical width of the resistive current layers fall below the ion skin-depth $d_i = c/\omega_{pi}$. Here c is the speed of light and ω_{pi} is the ion plasma frequency. In these narrow current layers the ions' inertia may cause them to decouple from the motion of the magnetic field which has been shown to have dramatic implications for the reconnection process.

To more accurately describe the narrow current layers of reconnection, two-fluid models treat the ions and the electrons as separate fluids and successfully predict both fast reconnection and the basic structure of the reconnection region observed in more advanced kinetic models⁵. The two-fluid reconnection geometry includes an ion diffusion region (IDR) with the width of about $1d_i$, and within this region the ion frozen-in condition is broken. Mathematically, this occurs when $\mathbf{E} + \mathbf{u}_i \times \mathbf{B} \neq 0$, where \mathbf{E} and \mathbf{B} denote the electric and magnetic fields, and \mathbf{u}_i is the ion bulk flow velocity. Meanwhile, the electrons with bulk flow \mathbf{u}_e remain frozen to the field line motion obeying the electron frozen-in law ($\mathbf{E} + \mathbf{u}_e \times \mathbf{B} = 0$) almost all the way into the topological X -line. Ultimately, the frozen-in law is also broken for the electrons within the much smaller electron diffusion region (EDR) with

a width of the order of the electron skin-depth, $d_e = c/\omega_{pe}$, where ω_{pe} is the electron plasma frequency. Numerical fluid models which fully resolve d_e often break the electron frozen-in law by adding an ad hoc amount of hyper-resistivity (scaling in strength with the Laplacian of the plasma current density, $\nabla^2 J$)⁶. An important result of this type of investigations was the realization that the rate of reconnection becomes insensitive to the physics that are responsible for decoupling the electrons from the motion of the magnetic field lines within the EDR⁷.

Despite substantial efforts including laboratory, spacecraft, numerical and theoretical investigations⁸, a complete understanding of the electron dynamics within the EDR is still not fully developed, and its study is complicated by the process being sensitive to a range of parameters describing a given configuration. Open questions are also concerned with the extent to which 3D effects fundamentally alter the structure of the reconnection region^{9–11}. However, observations from the Magnetospheric Multiscale (MMS) mission demonstrate that the widths of reconnection layers typically approach the small length scales associated with the local electron orbit width. The length scales perpendicular to a particular reconnection current layer are usually much shorter than the length scale along the current layer, and a range of observations further suggest that the local reconnection dynamics are well captured by 2D laminar models^{12–15}.

The present paper is focused on the case of 2D symmetric and anti-parallel reconnection, which observations suggest is applicable to reconnection in the Earth's magnetotail. Here, the opposing inflow regions often have similar strength magnetic fields but are oppositely directed¹⁶. Our numerical investigation also applies the typical ion to electron temperature ratio, $T_i/T_e = 5$, of the magnetosphere (see Ref.¹⁷, Fig.4);

the results are relatively insensitive to this ratio. Meanwhile, just a small guide-magnetic field in the direction of the current layer can significantly alter the reconnection process, and the present results (obtained with $B_g = 0$) only apply to cases where $B_g \leq 0.05B_{\text{rec}}$, corresponding to Regime I reconnection as introduced in Ref.¹⁸. While not explicitly imposed, the number densities of the electrons and ions are always similar, consistent with the condition of quasi-neutrality being well satisfied in the simulations. Thus, throughout the paper we will use $n_e = n_i \equiv n$.

Within the confines of the closed field lines of the plasma sheet in the Earth's magnetotail, the normalized electron pressure, $\beta_e = nT_e/(B/(2\mu_0)) \simeq 0.1$ is typical¹⁷. However, if reconnection persists for a sufficient duration, low- β_e plasma from the lobe regions outside the plasma sheet can reach the reconnection inflows. This can cause a dramatic drop in the plasma inflow density, reducing the electron pressure such that $\beta_e \ll 0.1$. For such low values of β_e , the reconnection dynamics change dramatically with the generation of strong electrostatic turbulence including colliding electron holes and double layers^{19,20}. In the present paper, the numerical simulations cover the range $0.008 \leq \beta_e \leq 0.5$, and the present work is thus limited to the conditions typically observed during symmetric reconnection in the plasma sheet.

For laminar and near steady state reconnection the force balance of the electron fluid is described by the generalized Ohm's law, which similar to the Navier-Stokes equation for a regular fluid includes pressure and inertial effects:

$$\mathbf{E} + \mathbf{u}_e \times \mathbf{B} + \frac{1}{ne} \nabla \cdot \mathbf{p}_e + \frac{m_e}{e} \mathbf{u}_e \cdot \nabla \mathbf{u}_e = 0 \quad (1)$$

Here the electron pressure tensor is computed by an integral over the electron phase-space density distribution, $\mathbf{p}_e = m_e \int (\mathbf{v}_e - \mathbf{u}_e)^2 f_e(\mathbf{v}_e) d^3v_e$, with \mathbf{v}_e representing the electron velocity. Using a range of kinetic simulations, in the present paper we will discuss how the various terms of Eq. (1) become important within separate spatial areas of the IDR and EDR. Compared to similar investigations a decade or more ago²¹⁻²³, a main difference is that modern computing facilities now permit routine fully kinetic simulations at the full proton to electron mass ratio, $m_i/m_e = 1836$. The present analysis reveals that for simulations where this ratio approaches its natural value, $\mathbf{E} + \mathbf{u}_e \times \mathbf{B} \simeq 0$ does not apply to the full IDR. The reconnection electric field, E_{rec} , is the electric field along the topological X -line at the center of the EDR, which by Faraday's law defines the rate at which magnetic flux is reconnected. For the inner part of the IDR (but still outside what is traditionally considered the EDR^{24,25}) we find that the $|E_{\text{rec}}| \ll |\nabla \cdot \mathbf{p}_e/(ne)|$ such that $\mathbf{u}_e \times \mathbf{B} \simeq -\nabla \cdot \mathbf{p}_e/(ne)$ becomes the main driver of the Hall magnetic field perturbation. In fact, the familiar assumption of $u_{\text{in}} = E_{\text{rec}}/B_{\text{rec,up}}$ significantly underestimates the inflow speed of the electron fluid into the EDR. Here, $B_{\text{rec,up}}$ is the in-plane magnetic field just upstream of the EDR.

The main topic of the paper, however, is the development of a theory to explain the terms of Eq. (1) which break the electron frozen-in condition at the very center of the EDR. The study emphasizes the importance of the electron anisotropy

upstream of the EDR in driving the current within the EDR and cancelling an off-diagonal stress term identified in previous work^{21,26}. Ultimately, the off-diagonal stress of \mathbf{p}_e , that is responsible for breaking the frozen-in condition, is generated by E_{rec} itself. Thus, the theory suggests that the electron fluid does not represent an obstacle (or bottleneck) for reconnection, which may then proceed at the rate imposed by dynamics external to the EDR. In turn, once reconnection has started, its rate will be controlled by larger scale dynamics which in many cases is well described by MHD models^{27,28}. In certain cases including island coalescence it can also be important to retain effects of ion pressure anisotropy^{29,30}.

The paper is organized as follows: In Section II we discuss previous results on the formation and role of electron pressure anisotropy within the IDR inflow regions, and how it drives the current of the EDR. Section III explores the structure and energy balance of electron flows within the inner part of the IDR, whereas Section IV examines the length scales characterizing the EDR. A detailed account of the electron momentum balance at the X -line region is provided in Section V, and the paper is summarized and concluded in Section VI.

II. SUMMARY OF PREVIOUS RESULTS ON THE ROLE OF ELECTRON PRESSURE ANISOTROPY

Our analysis relies strongly on previous results regarding the overall force balance of the EDR³¹⁻³³. For the convenience of the reader, in this section we provide a short summary of this previous work on how the upstream electron pressure anisotropy impacts the structure of the EDR. Additionally, in Appendices A and B we provide additional mathematical considerations to demonstrate how the upstream electron pressure anisotropy drives the current jets within the EDR.

A. Formation of electron pressure anisotropy in reconnection inflows, upstream of the EDR

Due to the trapped orbit dynamics illustrated in Fig. 1(a), it is generally found that the reconnection inflows are characterized by a regime of double adiabatic electron dynamics. It can be shown^{31,34} that at the upstream edge of the EDR the main electron pressure components are well described by the CGL-limit³⁵ with $p_{e\parallel} \propto n^3/B^2$ and $p_{e\perp} \propto nB$, where \parallel and \perp denote the directions parallel and perpendicular relative to the local direction of \mathbf{B} . For $\beta_{e\infty}^2 m_i/m_e \lesssim 1$ electron holes and double layers yield even stronger $p_{e\parallel}$ heating^{20,32}. The effects of the anisotropic heating are evident in the profile in Fig. 1(b), where $T_{e\parallel}/T_{e\perp} \simeq 4$ is observed just upstream of the EDR, and the marginal electron firehose condition is approached, $p_{e\parallel} - p_{e\perp} \simeq B^2/\mu_0$. Within the EDR the adiabatic invariance of the electron magnetic moments, $\mu = mv_{\perp}^2/(2B)$, break, leading to isotropization and pitch angle mixing. As a result, the electron pressure is approximately isotropic in the reconnection exhaust^{18,36}.

As described in Appendix A, the physical mechanisms which underpin the CGL-scalings can be understood through

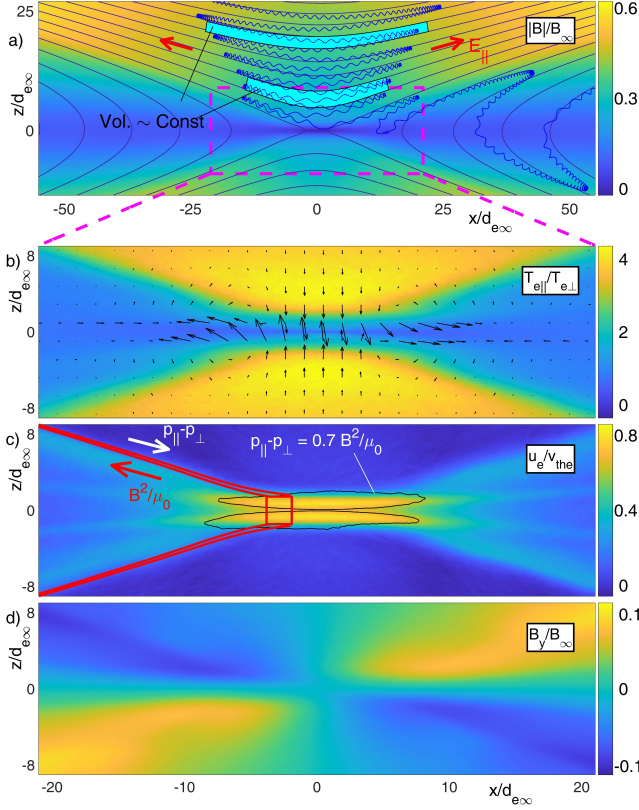


FIG. 1. VPIC simulations profiles of a) B/B_∞ , b) $T_{e||}/T_{e\perp}$, c) $|u_e|/v_{te}$, and d) B_y/B_∞ , obtained with $m_i/m_e = 1836$ and $\beta_{e\infty} = 2^{-4} = 0.0625$. The arrows in b) represent the enhanced electron flow provided by $\mathbf{J}_{\text{extra}} = [(p_{e||} - p_{e\perp})/B]\mathbf{b} \times \kappa$.

relatively simple arguments applicable to the electrons just upstream of the EDR, where the described trapping and parallel compression dynamics (see compressed trapped orbit in Fig. 1(a)) are strong enough to dominate the properties of the electron fluid. A more accurate and rigorous model is provided in^{32,34} taking into account that not all electrons become trapped. For the present paper, however, it is sufficient to assume that within the inflow regions the electron pressures approximately follow the aforementioned CGL-scaling laws. While the present simulations use open boundary conditions, the same trapped electron dynamics occur in simulations with periodic boundary conditions³⁷. In contrast to periodic conditions, however, the open system do not need to accommodate the large island of reconnected flux which gets stuck in the periodic reconnection exhausts. Thus, with open boundary conditions a larger fraction of the system is available for the reconnection dynamics³⁸.

B. Force balance along the length of the EDR and associated scaling laws for the electron pressure anisotropy

In Refs.^{31,39} it was demonstrated that the two dominant terms of Eq. (1) along the EDR are $\mathbf{u}_e \times \mathbf{B}$ and $(\nabla \cdot \mathbf{p}_e)/ne$.

Expressed in terms of the Maxwell stress tensor, $\mathbf{T} = (\mathbf{B}\mathbf{B} - B^2\mathbf{I})/(2\mu_0)$, we have $-enu_e \times \mathbf{B} \simeq \mathbf{J} \times \mathbf{B} = \nabla \cdot \mathbf{T}$, and momentum balance then requires that $\nabla \cdot (\mathbf{p}_e - \mathbf{T}) \simeq 0$. Considering the area encircled by the red square in Fig. 1(c), it can then be shown by the divergence theorem^{31,33} that at the upstream edge of the EDR the electron firehose condition must be approximately satisfied,

$$p_{e||}^{\text{edge}} - p_{e\perp}^{\text{edge}} \simeq B_H^2/\mu_0, \quad (2)$$

where B_H represents the magnetic field strength just upstream of the EDR (the direction of this field rotates along the upstream edge of the EDR into the Hall magnetic field explaining the subscript H). For example, for the red square in Fig. 1(c) the magnetic tension acting on the sides of the fluid element (corresponding to the integral over the element of the $-enu_e \times \mathbf{B}$ force) is offset by pressure anisotropy. Again, this is discussed in more detail in Appendices A and B.

We can derive important scaling laws for the level of pressure anisotropy for locations just upstream of the EDR. Using that $p_{e||}^{\text{edge}} \gg p_{e\perp}^{\text{edge}}$ with the CGL-limits the maximal pressure differential

$$\Delta p_{e||\perp}^{\text{max}} \equiv \max(p_{e||} - p_{e\perp}) = p_{e||}^{\text{edge}} - p_{e\perp}^{\text{edge}}, \quad (3)$$

adheres to the asymptotic scaling $\Delta p_{e||\perp}^{\text{max}} \simeq p_{e||}^{\text{edge}} \simeq (\pi\tilde{n}^3/(6\tilde{B}_H^2))\beta_{e\infty}B_\infty^2/(2\mu_0)$. The factor $\pi/6$ is part of the L^ê 2009 Equations of State³⁴, and the ∞ subscripts refer to quantities being evaluated far upstream of the IDR, where the electron pressure is assumed to be isotropic. The firehose condition in Eq. (2), representing the dominant momentum balance condition of the EDR, may then be expressed as

$$\frac{B_H}{B_\infty} = \frac{\mu_0 K}{2B_\infty} = \left(\frac{\pi\tilde{n}^3\beta_{e\infty}}{12} \right)^{1/4}. \quad (4)$$

Here K is the integral of the current density across the layer, representing the current per unit length of the EDR. $\tilde{n} \simeq 1$ is the local electron density normalized by the upstream value n_∞ (and similar for \tilde{B}_H used above)³¹. Eq. (4) is significant as it demonstrates how K is mainly controlled by the external electron pressure anisotropy, which through the CGL-like scalings is set by the normalized upstream electron pressure, $\beta_{e\infty}$.

The above result is in contrast to predictions of two-fluid models with isotropic pressure where $\mathbf{u}_e \times \mathbf{B}$ is balanced by resistive terms, \mathbf{E} , and/or $(m_e/e)\mathbf{u}_e \cdot \nabla \mathbf{u}_e$. As discussed below, the half-width $l_z \simeq 2d_{e\infty}$ of the EDR region current layer is set by the meandering orbit width⁴⁰⁻⁴². From Ampère's law it then follows that $B_H = \mu_0 enu_e l_z \simeq 2\mu_0 enu_e d_{e\infty}$, such that $u_e = B_H/(2enu_e d_{e\infty}) \simeq B_H/(2\sqrt{\mu_0 n m_e}) = v_{Ae}/2$. Thus, u_e must approach the corresponding value of $\sim v_{Ae}/2$, simply because of the narrow width of the current layer $l_z \simeq 2d_{e\infty}$. This analysis is also applicable to the Harris sheet type current layer and the condition $u_e = v_{Ae}/2$ is therefore reflective of the underlying meandering orbit dynamics setting the narrow width of the electron flow region⁴². The EDR current layer

direction rotates as a function of x in the xy -plane^{39,43,44}, and yields the B_y perturbations shown in Fig. 1(d)^{31,44}. The above results have also been applied in deriving scaling laws for the absolute electron heating within the reconnection inflow and EDR⁴⁵.

III. ELECTRON FLOWS AND ENERGY BALANCE WITHIN THE INNER PART OF THE IDR

A. Setup of kinetic simulations

The 2D kinetic simulations applied in our study were implemented for anti-parallel Harris sheet reconnection using the code VPIC⁴⁶ with open boundary conditions²². The initial magnetic field and the density are $B_x = B_0 \tanh(z/\lambda)$ and $n = n_0 \cosh^2(z/\lambda) + n_\infty$, respectively, where $\lambda = 0.5d_{i0} = 0.5\sqrt{\epsilon_0 m_i c^2 / n_0 e^2}$. Other parameters are initial uniform temperatures with $T_{i\infty}/T_{e\infty} = 5$, $\omega_{pe0}/\omega_{ce0} = 2$, and ~ 400 particles per species per cell. The study incorporates 35 separate simulation runs implementing a matrix of 5 values for m_i/m_e and 7 values for the normalized upstream electron pressure, $\beta_{e\infty}$. To be more specific, we use mass ratios of $m_i/m_e \in \{100, 200, 400, 800, 1836\}$, and the background density n_∞ is varied so the initial upstream electron beta is $\beta_{e\infty} = 2\mu_0 n_\infty T_{e\infty} / B_0^2 = 2^{-k}$ with $k \in \{1, 2, \dots, 7\}$. In VPIC “natural” units the systems are implemented using $m_e = 1$, $d_{e0} = 1$, $c = 1$, $n_0 = 1$, $B_0 = 1/2$, $T_{e\infty} = (1/48)m_e c^2$, and $n_\infty/n_0 = (1 + T_{i\infty}/T_{e\infty})2^{-k}$.

For runs with $m_i/m_e \leq 200$ the domains were 3960×1980 cells, corresponding to $50d_{ip} \times 25d_{ip}$. Runs at $m_i/m_e \geq 400$ were carried with 5632×2816 cells, corresponding to system sizes of $1000d_{ep} \times 500d_{ep}$. Here, d_{ip} and d_{ep} are the ion and electron skin-depths, respectively, defined with respect to the central peak Harris sheet density, $n_p = n_0 + n_\infty$. Furthermore, the upstream electron skin-depth becomes central to our analysis below and can be expressed as $d_{e\infty} = d_{e0}/\sqrt{n_\infty/n_0}$. For all of the runs, a fixed electron temperature is applied such that $v_{te}/c = 0.144 = L_{\text{Debye}}/d_{e0}$. Measuring the cell size, δ , relative to the Debye length, we then have $\delta/L_{\text{Debye}} \simeq (1000/5632) \cdot 0.144 \simeq 1.2$, again, based on the initial temperature. The computational cost of the runs scales approximately as $(m_i/m_e)(L_x/d_{ep})^2$. More details about the similarities and differences between the individual simulation runs are provided in Section IV, where the lengths and widths of the EDR electron jets are examined. In addition, in Table I of Appendix D we provide the simulation domain sizes normalized by various parameters.

B. The reconnection rate from the perspective of the electrons

Consistent with external MHD scale constraints for system sizes larger than $10d_{i\infty}$ ²⁸, in the present simulations the absolute reconnection rate obeys $E_{\text{rec}} \simeq \alpha v_A B$. Here $\alpha \simeq 0.1$ is the normalized reconnection rate, and the relevant Alfvén speed and B are evaluated $1d_i$ upstream of the EDR⁴⁷. In our study,

values of E_{rec} are computed through a spatial average of E_y over a $2d_{e\infty} \times 0.5d_{e\infty}$ region centered on the topological X -line. In Fig. 2(a), the corresponding values of α are shown for the full range of our simulations. It should be noted that for $m_i/m_e = 1836$ and $k = 7$ the numerical domain only measures about $5d_{i\infty} \times 2.5d_{i\infty}$ (see Table I.C in Appendix D). This could explain the slightly enhanced normalized reconnection rate of $\alpha \simeq 0.14$, which is expected as the “electron-only” regime is approached at small system sizes^{48–51}. Nevertheless, other runs in the set show similar values of α and, as will become clear below, the dynamics recorded for this most extreme run still conform well with the general trends of the full data set.

In Section IV we document how the size of the EDR normalized by $d_{e\infty}$ remains approximately constant for varying values of m_i/m_e . Meanwhile, the size of the IDR scales with $d_{i\infty} = d_{e\infty}\sqrt{m_i/m_e}$, and from the perspective of the electrons the size of the ion diffusion region thus increases by a factor of $\sqrt{m_i/m_e}$. Likewise, relative to the time scale of the electron motion, the increasing inertia of the ions will slow the rate of reconnection. As a dimensionless measure of the reconnection electric field relevant to the electron orbit dynamics we introduce $\hat{E}_{\text{rec}} = ed_{e\infty}E_{\text{rec}}/T_{e\infty}$. This quantity represents the temperature-normalized energy gain an electron will acquire when traveling $d_{e\infty}$ in the direction of E_{rec} . Corresponding to the data shown in Fig. 2(b), it then follows that $\hat{E}_{\text{rec}} \propto \sqrt{m_e/(m_i\beta_{e\infty}^2)}$, where reduced values of m_i/m_e and low $\beta_{e\infty}$ impose the largest values of \hat{E}_{rec} .

In Fig. 2(c) we show the profiles of $T_{e\parallel}/T_{e\infty}$ and $T_{e\perp}/T_{e\infty}$ corresponding to values in the various runs recorded just upstream of the electron diffusion region. Consistent with the discussion in Section II, for simulations within the double adiabatic regime ($\beta_{e\infty}^2 m_i/m_e \gtrsim 1$) marked by the full lines, we observe that both of these profiles are largely independent of m_i/m_e . The normalized electron pressure anisotropy $(p_{e\parallel} - p_{e\perp})/(n_\infty T_{e\infty})$ is then also independent of m_i/m_e , and given the scaling of $\hat{E}_{\text{rec}} \propto \sqrt{m_e/m_i}$ the forces associated with the pressure anisotropy become most significant when compared to $e\hat{E}_{\text{rec}}$ at large values of m_i/m_e . In fact, as illustrated in Fig. 2(d) and to be discussed further below, the thermal forces of the electron pressure anisotropy dominate the force balance of the electrons for $m_i/m_e = 1836$, rendering the electron dynamics of the IDR and EDR significantly different when compared to reduced fluid models invoking isotropic electron pressure.

C. Dominant role of $p_{e\parallel} \gg p_{e\perp}$ in setting the electron flows and energy dissipation upstream of the EDR

In the region outside the EDR where the electrons are well magnetized, the electron pressure anisotropy ($p_{e\parallel} \gg p_{e\perp}$) drives additional currents, $\mathbf{J}_{\text{extra}} = [(p_{e\parallel} - p_{e\perp})/B]\mathbf{b} \times \boldsymbol{\kappa}$, via the curvature drift; these currents are not observed for isotropic pressure³². Here $\boldsymbol{\kappa} = (\mathbf{b} \cdot \nabla)\mathbf{b}$ is the curvature vector, which becomes large where the magnetic field direction, $\mathbf{b} = \mathbf{B}/B$, has strong spatial variation. In Fig. 1(b) the arrows are proportional to $-\mathbf{J}_{\text{extra}}$ corresponding to a flow boosting the perpendicular drift of electrons into the EDR. $\mathbf{J}_{\text{extra}}$ also

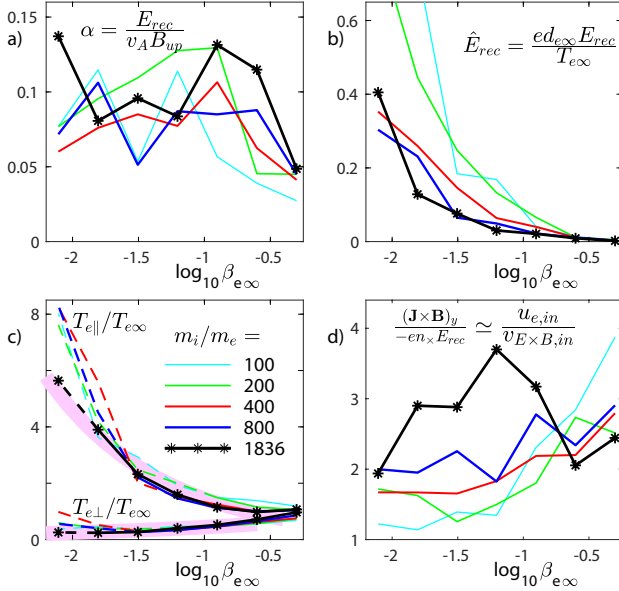


FIG. 2. Obtained from a matrix of 35 kinetic simulations, profiles as functions of $\log_{10}(\beta_{\infty})$ are shown for a range of parameters as marked in the panels. As indicated in c), the line-type denotes the value of m_i/m_e . The “ion-normalized” reconnection rate $\alpha = E_{\text{rec}}/(v_A B_{\text{up}})$ is shown on a) while in b) $\hat{E}_{\text{rec}} = e d_{\infty} E_{\text{rec}}/T_{\infty}$ is the normalized rate relevant to the electron dynamics. In c) the regions shaded in magenta are obtained from the CGL-limit of the Lê-2009 Equations of State³⁴. The dashed lines mark runs in the regime $\beta_{\infty} \lesssim \sqrt{m_i/m_e}$ where additional $T_{e\parallel}$ heating is typically observed^{20,45}. The profiles in d) show the maximum value of $(\mathbf{J} \times \mathbf{B})_y$ observed just upstream of the EDR, normalized by $-en_x E_{\text{rec}}$, documenting how forces related to $\mathbf{J} \times \mathbf{B}$ and $\nabla \cdot \mathbf{p}_e$ dominate at the natural value of m_i/m_e .

has a component in the y-direction which drives currents outside the EDR that are in the opposite direction of the electron current within the EDR. While the mathematical expression for $\mathbf{J}_{\text{extra}}$ is not valid inside the EDR, as discussed in Section II the out-of-plane electron current of the EDR can still be attributed to similar effects directly related to $p_{e\parallel} \gg p_{e\perp}$.

To quantify the relative importance of the flow by $\mathbf{J}_{\text{extra}}$, in Fig. 3 we provide additional profiles for the simulation of Fig. 1, here focusing on the force balance in the y-direction in the vicinity of the EDR. Within the IDR we generally have $(\mathbf{u}_e \times \mathbf{B})_y \gg (\mathbf{u}_i \times \mathbf{B})_y$ and we thus introduce the approximation that $(-en\mathbf{u}_e \times \mathbf{B})_y \simeq (\mathbf{J} \times \mathbf{B})_y$. Consistent with previous work⁵², generally we have that $|(\mathbf{J} \times \mathbf{B})_y| \gg |(enm_e \mathbf{u}_e \cdot \nabla \mathbf{u}_e)_y|$, and the y-component of the electron inertia can for the present analysis be neglected. With these approximations the y-component of the generalized Ohm’s law in Eq. (1) then becomes⁵³

$$-enE_y + (\mathbf{J} \times \mathbf{B})_y = (\nabla \cdot \mathbf{p}_e)_y \quad (5)$$

For the time point considered in Fig. 3 the reconnection geometry and rate is approximately steady. Furthermore, the density profile in this inner region is approximately uniform at a density we denote as n_{\times} . It then follows that $nE_y \simeq n_{\times} E_{\text{rec}}$,

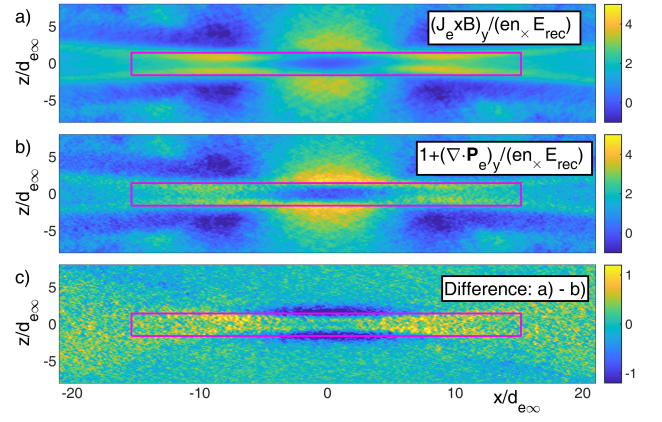


FIG. 3. Considering the same simulation as in Fig. 1 ($m_i/m_e = 1836$ and $\beta_{\infty} = 2^{-4}$), color contours are presented for a) the LHS and b) RHS of Eq. (6). The EDR is outlined by the magenta rectangles. For the extended regions where $(\mathbf{J} \times \mathbf{B})_y/(n_{\times} E_{\text{rec}}) \gtrsim 3.5$ the electron fluid is moving faster than the magnetic field. This motion is driven by electron pressure anisotropy such that $|\mathbf{J} \times \mathbf{B}| \simeq |\nabla \cdot \mathbf{p}_e| \gg en_{\times} E_{\text{rec}}$. The difference between panels a) and b) is shown in c) and can be attributed to the neglected electron inertia term (note the change in color scale).

where E_{rec} is the value of E_y observed at the X-line. After dividing Eq. (5) by $en_{\times} E_{\text{rec}}$ we obtain:

$$\frac{(\mathbf{J} \times \mathbf{B})_y}{en_{\times} E_{\text{rec}}} \simeq 1 + \frac{(\nabla \cdot \mathbf{p}_e)_y}{en_{\times} E_{\text{rec}}} \quad (6)$$

The LHS (left hand side) of Eq. (6) is shown in Fig. 3(a), while the RHS is shown in Fig. 3(b). The difference between the profiles is relatively small and is shown in Fig. 3(c). This difference can be attributed to the neglected electron inertia in Eq. (6).

From Fig. 3(a) it is apparent that in the vicinity of the EDR $(\mathbf{J} \times \mathbf{B})_y$ is significantly larger than $en_{\times} E_{\text{rec}}$. Thus, rather than $enE_y \simeq (\mathbf{J} \times \mathbf{B})_y$, we see that $|enE_y| \ll |(\mathbf{J} \times \mathbf{B})_y| \simeq |(\nabla \cdot \mathbf{p}_e)_y|$ in the important inner part of the IDR and throughout most of the EDR. Within the IDR for $x = 0$, it is readily shown that $(\mathbf{J} \times \mathbf{B})_y/en_{\times} E_{\text{rec}} = u_{e,z}/v_{E \times B,z}$, and the enhanced inflow is provided by $p_{e\parallel} \gg p_{e\perp}$ through the drifts associated with $\mathbf{J}_{\text{extra}}$. In other words, while E_y by Faraday’s law is fundamental for moving the magnetic flux across the reconnection region, Fig. 3 reveals how the $(\nabla \cdot \mathbf{p}_e)_y$ -term is responsible for driving the electrons into the EDR and through the elongated jets of the EDR at high rates, which for the present run are up to 3.5 times the speed of the magnetic field line motion. In Fig. 2(d) the maximum value of $(\mathbf{J} \times \mathbf{B})_y/en_{\times} E_{\text{rec}} (= u_{e,z}/v_{E \times B,z})$ is shown for each of the runs, demonstrating how the enhancement of the inflow speed becomes most pronounced as $m_i/m_e = 1836$ is approached.

The electron pressure anisotropy also has implications for the energy dissipation within the reconnection region. It was recently emphasized⁵⁴ that an electron fluid obeying the frozen-in condition, $\mathbf{E} = -\mathbf{v}_e \times \mathbf{B}$, does not exchange any energy with the electromagnetic fields simply because $\mathbf{J}_e \cdot \mathbf{E} = en\mathbf{v}_e \cdot (\mathbf{v}_e \times \mathbf{B}) = 0$. This observation is altered by the pres-

ence of the strong electron pressure anisotropy. For this case $\mathbf{E} = -\mathbf{v}_e \times \mathbf{B} - \nabla \cdot \mathbf{p}_e / (ne)$, such that the now non-zero value of $\mathbf{J}_e \cdot \mathbf{E} = \mathbf{v}_e \cdot (\nabla \cdot \mathbf{p}_e)$ permits energy to be exchanged with the fields. In Fig. 4(a) we display the profile of $-\mathbf{J}_e \cdot \mathbf{E}$, where “yellow” areas with $-\mathbf{J}_e \cdot \mathbf{E} > 0$ are regions where the electrons give energy back to the fields. Such regions, known as generator regions, have been directly observed by the MMS mission⁵⁵.

The continuity of the electromagnetic energy is described by Poynting’s theorem, $-\partial u_{EB} / \partial t = \nabla \cdot \mathbf{S} + \mathbf{J} \cdot \mathbf{E}$, where $u_{EB} = \epsilon_0 E^2 / 2 + B^2 / (2\mu_0)$ is the electromagnetic field energy density and $\mathbf{S} = \mathbf{E} \times \mathbf{B} / \mu_0$ is the Poynting flux. The profile of $\nabla \cdot \mathbf{S}$ is shown in Fig. 4(b), which closely resembles the profile of $-\mathbf{J}_e \cdot \mathbf{E}$. The difference in Fig. 4(c) is the energy either exchanged with u_{EB} and/or the ions through $\mathbf{J}_i \cdot \mathbf{E}$. The smallness of this difference is consistent with a steady state scenario with steady energy density of the fields throughout the region.

As indicated above, the identified generator regions just upstream of the EDR are a direct consequence of the electron pressure anisotropy that develops in the inflow regions. This is emphasized when comparing $-\mathbf{J}_e \cdot \mathbf{E}$ in Fig. 4(a) with $-\mathbf{J}_{\text{extra}} \cdot \mathbf{E}_z$ in Fig. 4(d). Again, the expression for $\mathbf{J}_{\text{extra}}$ is not valid within the EDR. Nevertheless, the predicted values of $\mathbf{J}_{\text{extra}} \cdot \mathbf{E}_z$ demonstrate that the main contributor to $\mathbf{J}_e \cdot \mathbf{E}$ at the edge of the EDR are the curvature-drift-driven currents that enhance the inflow of the electrons into the strong E_z electric fields on the EDR’s edge. The structure of E_z will be discussed in further details below.

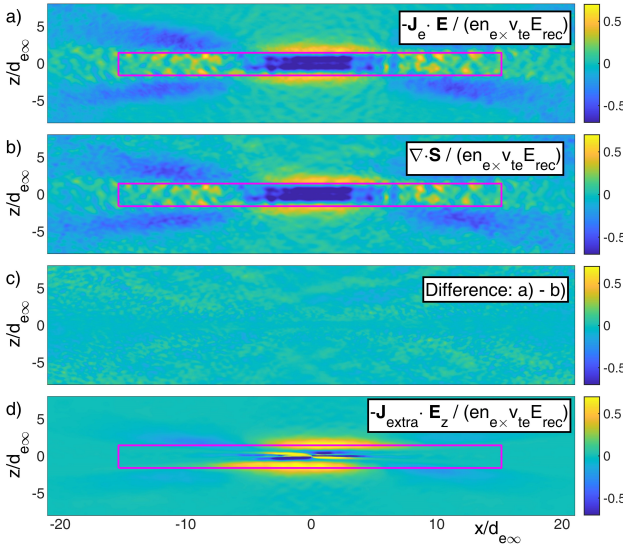


FIG. 4. a,b) Near identical profiles of $-\mathbf{J}_e \cdot \mathbf{E}$ and $\nabla \cdot \mathbf{S}$, representing the main two terms in Poynting’s theorem. Their difference is shown in c). The profile of $-\mathbf{J}_{\text{extra}} \cdot \mathbf{E}_z$ is shown d).

IV. LENGTH SCALES OF THE EDR

We now introduce a new length l_u , which is a measure of the spatial scale at which the direction of the out-of-plane EDR electron current at the X-line rotates into the exhaust direction. This length scale turns out to be fundamental our momentum balance analysis of the EDR.

A. Numerical evidence that l_u does not scale with simulation system size

In Ref.²², which employed relatively low mass ratio $m_i/m_e = 25$, it was observed that the length of the EDR increases with the size of the numerical simulation domain, and evidence was presented that the long electron current layers of the EDR could act as a bottleneck for reconnection. These results do not apply to our present simulations where m_i/m_e approaches its natural value of 1836. For example, in Fig. 5(a) profiles of u_{ex} are shown for a simulation at $m_i/m_e = 800$ and $\beta_{e\infty} = 2^{-4}$ for the “standard” setup described in Section II.A, whereas Figs. 5(b,c) apply domains factors of $2\times$ and $4\times$ larger, respectively. Zoomed-in views of the EDRs for the three runs are shown in Figs. 5(d-f). In the standard case the length of the EDR is likely reduced due to the proximity of the simulation boundaries, whereas we notice how the $2\times$ and $4\times$ runs have longer EDR lengths. This indicates that for simulations at large m_i/m_e , the length of the EDR becomes independent of the system size when the run is implemented in a sufficiently large domain.

For the analytical analysis of the EDR the following definition of l_u becomes essential to the presented theory for the force balance of the electron fluid. Here

$$l_u \equiv \left| \frac{u_{ey}}{du_{ex}/dx} \right|_{\text{X-line}}, \quad (7)$$

represents a measure of the spatial distance that characterizes the rotation of the EDR electron current direction in the xy -plane as a function of x . Figs. 5(g-i) provide the geometric interpretation of this quantity, which is observed to be on the order of $20d_e$ for the three runs. Below we show how l_u is significantly shorter than the full length l_{jet} of the EDR for many runs in our study, consistent with previously observed two-scale EDR structures^{24,25}.

B. Numerical results for l_u over the full $(\beta_{e\infty}, m_i/m_e)$ -matrix of kinetic runs

Fig. 6 provides zoomed-in views of the EDRs recorded in the full set of runs applied in our study. As is typical for kinetic simulations of reconnection based on the Harris sheet geometry, after fast reconnection has commenced the reconnection rate initially increases and then reduces to a near steady state. Each of the profiles considered here correspond to times $t \simeq 70\Omega_{ci}^{-1}$ during these later intervals of mostly steady state reconnection geometries. For $\beta_{e\infty} \geq 2^{-2}$ elongated EDRs are

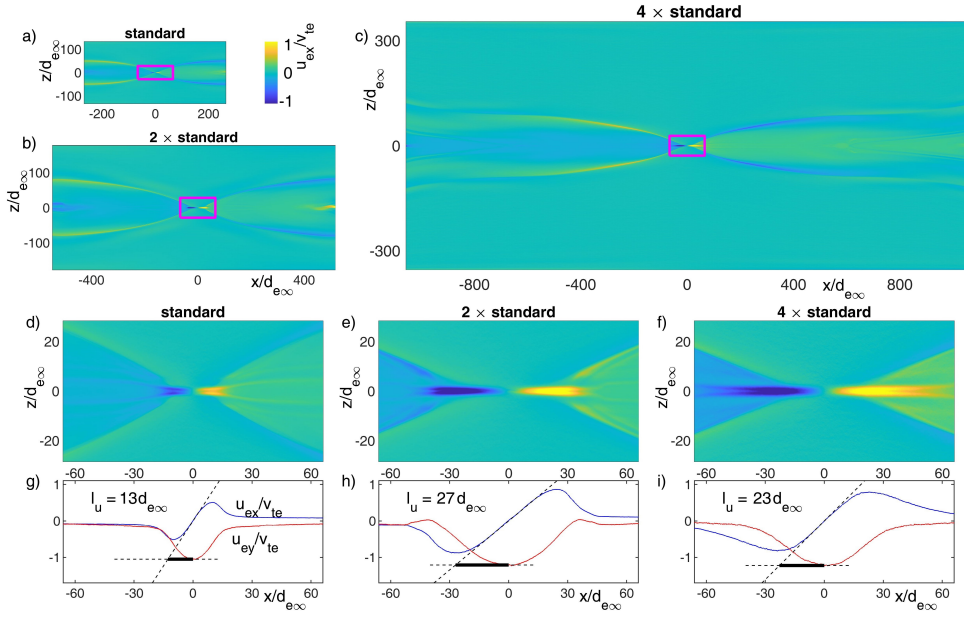


FIG. 5. a-c) Profiles of u_{ex}/v_{te} for the full simulation domains for three separate runs at $\beta_{e\infty} = 2^{-4}$ and $m_i/m_e = 800$. The run in a) has the “standard” size described in Section II.A, whereas the runs in b,c) are for simulations with spatial domain sizes increased by factors $2\times$ and $4\times$, respectively. Zoomed-in views of the EDRs are shown in d-f), whereas g-i) show cuts of u_{ex} and u_{ey} for $z = 0$, from which the length scale l_u of current layer rotation is determined.

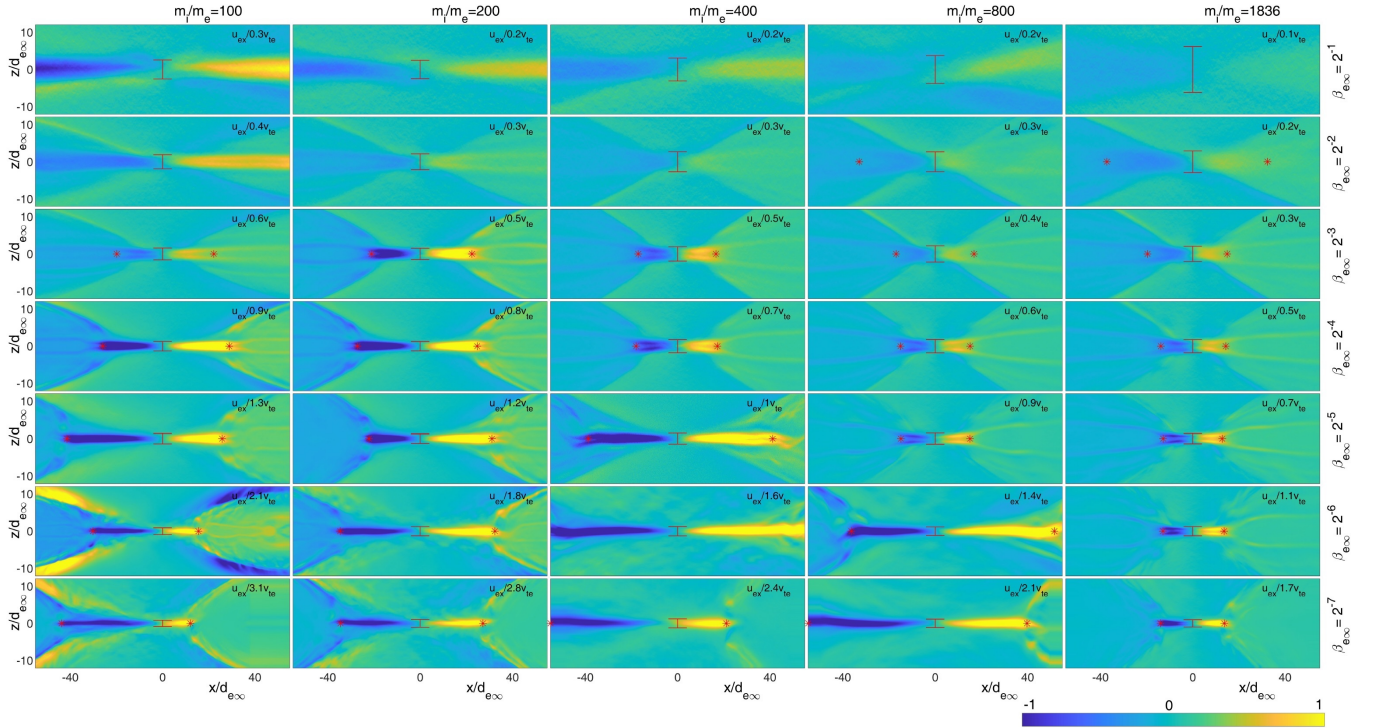


FIG. 6. Color contours of u_{ex} for the matrix of numerical simulations applied in the study, $m_i/m_e \in \{100, 200, 400, 800, 1836\}$ and $\beta_{e\infty} = 2^{-k}$ with $k \in \{1, 2, \dots, 7\}$. When falling within the domains considered, the ends of the jets are marked by the red stars corresponding to $|u_{ex}|$ dropping to 60% of its peak value. The similarly defined width of the u_{ey} out-of-plane electron drift is marked in each panel at $x = 0$.

mostly observed where $l_{jet} > 100d_{e\infty}$. Here the out-of-plane electron flows are largely provided by the diamagnetic drifts similar to those of the Harris sheet. Meanwhile, for $\beta_{e\infty} \leq 2^{-3}$, the force balance condition of the EDR as expressed in Eq. (4) requires current densities boosted beyond those provided by the diamagnetic effect, and the EDRs acquire a shorter length. The marked ends of the jets are defined by the locations where

$|u_{ex}|$ has fallen to 60% of its respective peak value. For the adiabatic regime ($\beta_{e\infty}^2 m_i/m_e \gtrsim 1$), the lengths of the electron diffusion region are consistently observed to be $l_{jet} \approx 20d_{e\infty}$. For the regime $\beta_{e\infty}^2 m_i/m_e \lesssim 1$ of enhanced $p_{e\parallel}$ energization²⁰, a sharp transition occurs where the EDRs are characterized by longer outflow jets.

In Fig. 7 we show the values of l_u and l_{jet} for all the runs ap-

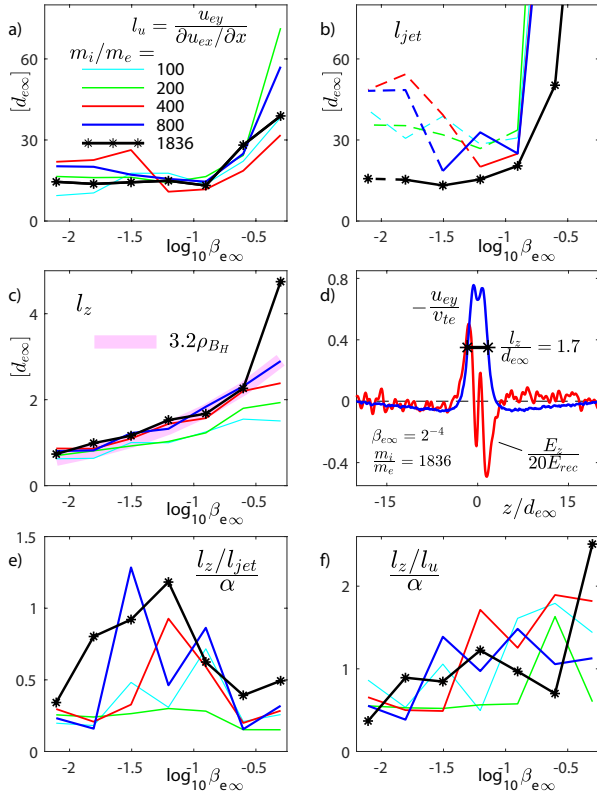


FIG. 7. a,b) Recorded values of l_u and l_{jet} , which are similar to the inner and outer lengths of the EDR introduced in Refs.^{24,25}. In b) the dashed lines indicate runs in the non-adiabatic regime with enhanced $p_{e\parallel}$ -heating observed for $\beta_{e\infty}^2 m_i/m_e \lesssim 1$. Evidently, this regime is also characterized by an enhancement in the length of the EDRs (while l_u remains near constant). c) Half-width of the electron current layer, which approximately scales as $3.2 \rho_{BH}$. Here ρ_{BH} is the typical electron Larmor radius at the upstream edge of the EDR. d) Considering the run with $m_i/m_e = 1836$ and $\beta_{e\infty} = 2^{-4}$, the blue line is $-u_{ey}/v_{te}$, while the red line shows the profile of E_z . The black line (full-width) indicates how l_z = half-width-half-maximum is obtained from $-u_{ey}/v_{te}$. e,f) Characteristic aspect ratios of the EDR, l_z/l_{jet} and l_z/l_u , compared to the normalized reconnection rate $\alpha = E_{rec}/(v_A B)$.

plied in the study. The runs with $\beta_{e\infty} \leq 2^{-3}$ (most relevant to the analysis in Section IV) are all characterized by $l_u \simeq 18d_{e\infty}$. In Fig. 7(b) the dashed lines represent runs in the aforementioned regime $\beta_{e\infty}^2 m_i/m_e \lesssim 1$ of enhanced $p_{e\parallel}$ heating, and it is evident that this regime is characterized by larger values of l_{jet} .

C. How continuity of electrons in the EDR sets the l_u length scale

Directly related to \mathbf{J}_{extra} , we find that l_u is shortened by the enhancement of the electron flow into the EDR. Let u_{ey0} be the flow in the y-direction at the X-line; given the definition of l_u the flow in the x-direction is then $u_{ex} = u_{ey0}x/l_u$. For a

uniform inflow velocity u_{ez} mass continuity requires that

$$nu_{ez}x = nu_{ex}l_z = nu_{ey0}xl_z/l_u$$

where l_z is the half width of the EDR analysed below. Carrying on, it follows that

$$l_u = \frac{u_{ey0}l_z}{u_{ez}} = \frac{B_H}{en\mu_0 u_{ez}}.$$

Meanwhile, the strong parallel streaming of electrons in toward the EDR causes the inflow speed of the electrons to increase. Empirically we find

$$u_{ez} \simeq 3.5E_{rec}/B_H.$$

This enhancement of the inflow speed above E_{rec}/B_H is caused by the inflow pressure anisotropy through the term $\mathbf{J}_{\perp extra}$, and is consistent with the profiles in Figs. 12(a,b).

As discussed above, the reconnection electric field, E_{rec} adhere to the scaling laws of Ref.⁴⁷ where

$$E_{rec} \simeq 0.1v_A B_{1di} = \frac{0.1B_{1di}^2}{\sqrt{\mu_0 n m_i}}.$$

It then follows that

$$l_u \simeq \frac{B_H^2}{0.35B_{1di}^2} \sqrt{\frac{m_i}{m_e}} d_e.$$

Empirically and consistent with Fig. 1(a), the magnetic field $1d_i$ upstream of the EDR is approximately $B_{1di} \simeq B_{\infty}/2$. Furthermore, due to non-adiabatic effects B_H depends on m_i/m_e (see Fig. 10(a)), and the scaling is consistent with $B_H^2 \sqrt{m_i/m_e}/(0.35B_{1di}^2) \simeq 17$ for all the runs. This scaling is also in agreement with recent results in Ref.⁵⁴. In turn, this is in reasonable agreement with the observation that $l_u \simeq 18d_{e\infty}$ in Fig. 7(a). It should be noted that l_u varies within the duration of a single simulation, but its precise length does not impact the qualitative predictions of the theory being presented below.

D. The half-width, l_z , of the EDR

The width of the EDR has previously been determined to scale with the orbit width of the meandering electrons^{40–42}; that result is also consistent with the simulations presented here. In Fig. 7(c), the half-width l_z is shown for each of the simulations. As illustrated in Fig. 7(d), we define l_z as the half-width where the half-maximum of the electron u_{ey} flow velocity is recorded for $x = 0$. We note that the simple approximation $l_z \simeq 2d_{e\infty}$ represents a reasonable estimate; this is especially true for the normalized electron pressures most typical in the Earth's magnetotail, $\beta_{e\infty} \simeq 0.1$.

More accurately, the meandering orbit width of the electrons is related to the electron Larmor radius at the upstream edge of the EDR, $\rho_{BH} = \sqrt{2m_e T_{e\perp}/(eB)}$, and can be estimated

using $B = B_H$ in Eq. (4), and $T_{e\perp} = T_{e\infty} B_H / B_\infty$. Thus, we then find

$$\rho_{B_H} = d_{e\infty} \left(\frac{B_\infty}{B_H} \beta_{e\infty} \right)^{\frac{1}{2}} = d_{e\infty} \left(\frac{12}{\pi} \right)^{\frac{1}{8}} \beta_{e\infty}^{\frac{1}{4}}. \quad (8)$$

The thick magenta line in Fig. 7(c) represents $3.2\rho_{B_H}$ and provides a good approximation for l_z for the runs at $\beta_{e\infty} \leq 2^{-2}$ and $m_i/m_e \geq 400$. At the lowest values considered for $\beta_{e\infty}$, however, it is observed that $3.2\rho_{B_H}$ underestimates l_z . This slightly weaker scaling of l_z as a function of $\beta_{e\infty}$ may in part be explained by the fact that a fraction of the u_{ey} -drift is caused by the $E \times B$ -drift of the strong E_z field at the upstream edge of the EDR. This field is illustrated by the red line in Fig. 7(d) and the color profile in Fig. 8(a); for all the runs we find that the width of this E_z -structure is fixed when normalized by $d_{e\infty}$ (not shown).

Due to the strong drift provided by $\mathbf{J}_{\text{extra}}$ and because the currents inside the EDR are being driven by $p_{e\parallel} - p_{e\perp}$, it is not mathematically guaranteed that the aspect ratio of the EDR is directly related to the normalized reconnection rate α discussed above and shown in Fig. 2(a). Therefore, in Figs. 7(e,f) we show the recorded values of l_z/l_{jet} and l_z/l_u both normalized by α . In particular, it is observed that $(l_z/l_u) \simeq \alpha$ for most of the runs with $m_i/m_e \geq 400$. This quantity may then be useful for estimating the normalized reconnection rate from spacecraft observations⁵⁶.

V. BREAKING THE FROZEN-IN LAW AT THE RECONNECTION X-LINE

The major force terms of the EDR are $\mathbf{J} \times \mathbf{B}$ and $\nabla \cdot \mathbf{p}_e$ which largely balance. As discussed above this force balance requirement can ultimately be expressed through the conditions in Eqs. (2) or (4). However, as seen in Fig. 3(a), in a small region ($4d_e \times 2d_e$) centered on the X-line the $(\mathbf{J} \times \mathbf{B})_y$ force vanishes, such that the more detailed force balance right at the X-line then requires that the RHS of Eq. (6) also vanishes (consistent with Fig. 3(b)). Thus, for the considered anti-parallel and symmetric configurations and within this limited region around the X-line, the force balance constraint of Eq. (1) only involves the off-diagonal stress in the electron pressure tensor⁵³:

$$E_{\text{rec}} = -\frac{1}{en} \left(\frac{\partial p_{exy}}{\partial x} + \frac{\partial p_{eyz}}{\partial z} \right). \quad (9)$$

Again, here E_{rec} is the E_y electric field along the X-line (that is aligned with the y axis and runs through $(x, z) = (0, 0)$). By Faraday's law E_{rec} then represents the rate at which magnetic flux crosses the X-line. Below we will derive a new model for the terms in Eq. (9), providing a theory consistent with fast reconnection controlled by larger scale dynamics external to the EDR.

A. Meandering orbit motion of electrons within the EDR, setting the striated structure of the electron distribution function

To elucidate how the upstream electron pressure anisotropy drives the current of the EDR, in Fig. 8 we consider the trajectories of electrons with field-aligned velocities $\mathbf{v} = 3.3v_{te}\mathbf{B}/B$ injected with $z = -4d_{e\infty}$ at various values of $x < 0$ just upstream of the EDR. Here $v_{te} = \sqrt{T_e/m_e}$ is the electron thermal speed. The trajectories, computed through integration of the equations of motion with a Matlab ODE solver in the simulation fields, are representative because the upstream distributions (like in Figs. 9(a,d)) with $p_{e\parallel}^{\text{edge}} \gg p_{e\perp}^{\text{edge}}$ “feed” electrons to the EDR with $|v_{\parallel}| \gg v_{\perp}$ ⁵⁷. In Figs. 8(a,b) the parts of the trajectories with $z < 0$ ($z > 0$) are represented by the blue (red) full lines. To better illustrate the orbit morphology, for each transit across $z = 0$ in Fig. 8(b) additional orbits are initialized and shown by the dashed lines. This visualizes how the average force of $-e\mathbf{v} \times B_z \mathbf{e}_z$ causes the meandering Speiser-type motion⁵⁸ to diverge away from the X-line.

The EDR current is caused in part by the $E \times B$ -drift of the E_z field displayed in Fig. 8(a). The large values of E_z are consistent with momentum balance with the strong gradients of p_{\parallel} at the interface of the EDR. The initial blue section of the trajectories in Fig. 8(b) are aligned with the magnetic field at the upstream edge of the EDR. Thus, the direction of the parallel thermal streaming is sensitive to the B_y Hall magnetic field, which thereby sets the angle in the xy -plane at which the electrons are injected into the EDR region.

In Figs. 8(c-e) the colored and encircled triangles represent the particle velocities corresponding to the similarly colored velocity vectors in Fig. 8(b). For example, the magenta vector at $x = 0$ in Fig. 8(b) pointing mostly in the x -direction, yields the velocity of an electron reaching the X-line directly from the upstream region, and the corresponding encircled magenta triangle in Fig. 8(d) has $|v_x| \gg |v_y|$. The X-line may also be reached through multiple meandering motions within the layer, steadily directing the velocity into the $-y$ -direction. As shown in Figs. 8(c-e), repeating this procedure for four more initial velocities $\mathbf{v} = v_{\parallel}\mathbf{B}/B$ within the interval $0.1 \leq v_{\parallel}/v_{te} \leq 3.3$ yields the lines of colored triangles, corresponding to the centers of the striated structures of the EDR electron distributions first described in Ref.⁵⁷. In Figs. 8(c-e), the similar points marked by green circles are the result of injecting electrons along field lines from the opposing inflows of the EDR. Also, going from $x/d_{e\infty} = -3$ to $x/d_{e\infty} = 3$, we note how the displayed structures rotates in the $v_x v_y$ -plane (and similarly in Fig. 9), corresponding to the rotation of the EDR current layer direction mentioned above^{57,59}, and parameterized by l_u .

B. Origin for the off-diagonal $\partial p_{exy}/\partial x$ -stress at the reconnection X-line

To understand how the upstream pressure anisotropy influences p_{exy} we consider the electron distributions in Fig. 9. At the upstream edge of the EDR we have $p_{eyy} \simeq p_{ezz}$, and given

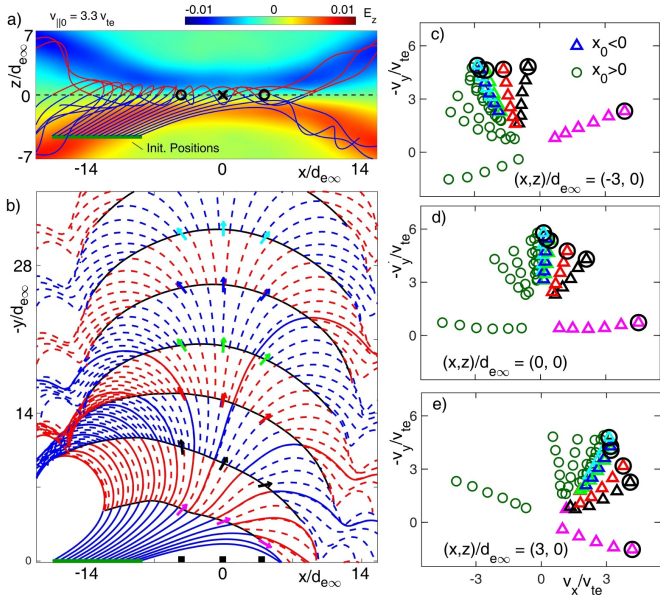


FIG. 8. a,b) Trajectories of electrons injected along field lines into the EDR with $v_{\parallel} = 3.3v_{te}$. Three points, $(x, z)/d_{e\infty} = (-3, 0); (0, 0); (3, 0)$, are selected in a) indicating the spatial locations where the velocity arrows in b) are evaluated. As indicated, the panels c-e) also correspond to these locations. The angles indicated by arrows in b) at which the trajectories reach the selected points, determine the location of the encircled triangles in c), d), and e), respectively. Similar trajectories are obtained by using a range of initial v_{\parallel} values and result in the striated structures marked by the symbols in c), characteristic of the EDR distributions⁵⁷ and observed in Fig. 9.

Eq. (3) it follows that $p_{eyy} - p_{exx} = -\Delta p_{e\parallel\perp}^{\max}$. Comparing the distributions in Figs. 9(a,b)) it is clear that only a fraction of this upstream anisotropy is carried by the orbit motion to the X-line. Empirically at the X-line we find that

$$(p_{eyy} - p_{exx})|_{X\text{-line}} = -\frac{4}{5}\Delta p_{e\parallel\perp}^{\max} + \Delta p_{eyy,E} \quad (10)$$

The lines in Fig. 9(b)) are drawn in “by eye” to indicate the center line of the striations in the (v_x, v_y) -plane, corresponding to electrons reaching the X-line without bounces across $z = 0$. The factor of 4/5 can be understood by noting the $\sim 42^\circ$ angle between these lines, which is double the angle at which the electrons are launched (by the ratio of B_y/B_x) as they initially enter the EDR. The change in the straight distribution just upstream of the EDR (with $\Delta p_{e\parallel\perp}^{\max}$) into the distribution with each side “bent in the middle” by 21° then yields a simple estimate for the relative reduction in $p_{exx} - p_{eyy}$:

$$\frac{(p_{exx} - p_{eyy})|_{X\text{-line}}}{\Delta p_{e\parallel\perp}^{\max}} = \cos^2(21^\circ) - \sin^2(21^\circ)/4 \simeq 0.84 \quad .$$

The phase space density of the striations for the higher bounce numbers mainly add to p_{eyy} , explaining the further reduction in the ratio towards 4/5.

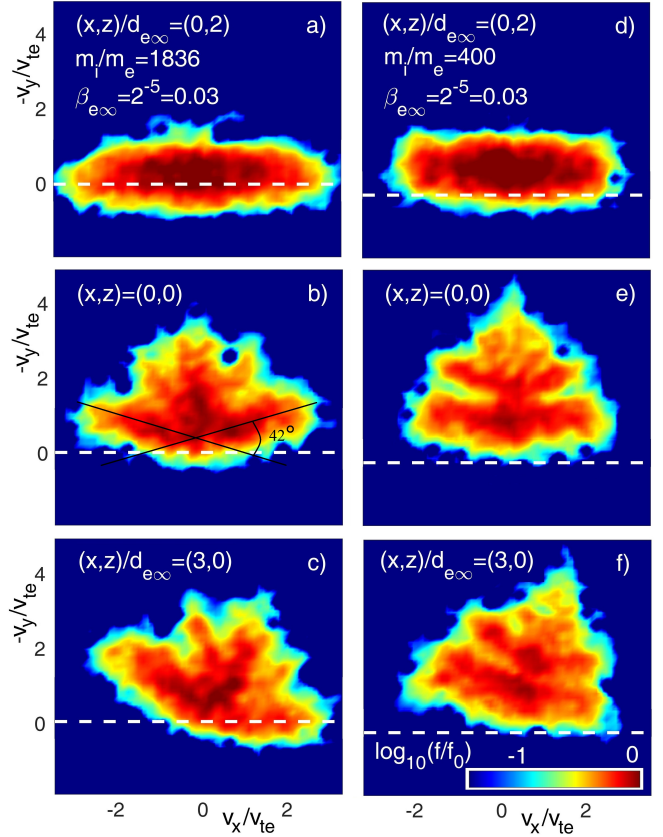


FIG. 9. Projections, $f_{xy}(v_x, v_y) = \int f(\mathbf{v}) dv_z$ of EDR electron distributions, recorded in simulations for $m_i/m_e = 1836$ in a-c) and $m_i/m_e = 400$ in d-f). The differences between the profiles are consistent with enhanced $\Delta p_{eyy,E}$ for $m_i/m_e = 400$, caused by $\hat{E}_{rec,400} \simeq 2\hat{E}_{rec,1836}$.

The additional term, $\Delta p_{eyy,E}$, in Eq. (10) corresponds to an increase in p_{eyy} due to direct heating of electrons by the reconnection electric field. From Fig. 8 it is clear that the “tips” of the triangular shaped distributions are composed of electrons meandering multiple times while streaming mostly in the $-y$ -direction, energized most significantly by \hat{E}_{rec} . The more pronounced triangular shapes in Figs. 9(e,f) compared to Figs. 9(b,c) are consistent with stronger $\Delta p_{eyy,E}$ heating, as the value of \hat{E}_{rec} for $m_i/m_e = 400$ is about twice as large compared to that observed in the $m_i/m_e = 1836$ run.

As detailed with Figs. 8 and 9, within the EDR the xy -projections of the electron distributions rotate approximately as a “solid-body”^{57,60} such that for small x/l_u

$$p_{exy} = \frac{x}{l_u} (p_{eyy} - p_{exx})|_{X\text{-line}} \quad . \quad (11)$$

Combining Eqs. (10) and (11) we then obtain

$$\frac{\partial p_{exy}}{\partial x} = \frac{1}{l_u} \left(-\frac{4}{5}\Delta p_{e\parallel\perp}^{\max} + \Delta p_{eyy,E} \right) \quad . \quad (12)$$

C. Origin for the off-diagonal $\partial p_{eyz}/\partial z$ -stress at the reconnection X-line

In the present paper we do not provide a formal derivation of the $\partial p_{eyz}/\partial z$ -stress. However, the first term in Eq. (12) is independent of E_{rec} as it is imposed by the upstream pressure anisotropy. The motion of each electron in the X-line region is naturally governed by Newton's laws, and once all forces are summed up over the electrons in a fluid element, the terms independent of E_{rec} must cancel in order for the fluid to be in force balance. Thus, force balance at the X-line requires that the $\partial p_{exy}/\partial x$ stress imposed externally is cancelled by an opposite term in Eq. (9). The only term available for this cancellation is $\partial p_{eyz}/\partial z$, and this simple argument then suggests that

$$\frac{\partial p_{eyz}}{\partial z} = \frac{1}{l_u} \frac{4}{5} \Delta p_{e\parallel\perp}^{\text{max}}. \quad (13)$$

Some theoretical support for Eq. (13) can be derived from the results in Refs.^{21,26}, which also obtained approximations for the off-diagonal pressure tensor derivatives ($\partial p_{exy}^{\text{Hesse}}/\partial x$ and $\partial p_{eyz}^{\text{Hesse}}/\partial z$).

$$\frac{\partial p_{exy}^{\text{Hesse}}}{\partial x} = \frac{\partial p_{eyz}^{\text{Hesse}}}{\partial z} = n \sqrt{\frac{m_e T_e}{2}} \frac{\partial u_{ex}}{\partial x}.$$

These were derived through an assumption of isotropic upstream electron pressure. As such, given that upstream of the EDR $p_{exx} - p_{eyy} = \Delta p_{\parallel\perp}$ is large, the $\partial p_{exy}^{\text{Hesse}}/\partial x$ -approximation is inaccurate and is not consistent with the simulation data presented below. In contrast, the conditions required for the accuracy of $\partial p_{eyz}^{\text{Hesse}}/\partial z$ are well satisfied, as the upstream pressure in the yz -plane is isotropic, $p_{eyy} \simeq p_{ezz} \simeq p_{e\perp}^{\text{edge}}$. Still, we find that a scale-factor must be applied, $\partial p_{eyz}/\partial z \simeq 3.6 \partial p_{eyz}^{\text{Hesse}}/\partial z$, for matching our numerical results at $m_i/m_e = 1836$ and $\beta_{e\infty} \leq 2^{-4}$ (see below).

Using the result above that the width of the EDR is $l_z \simeq 3.2 \rho_{BH}$, from Ampère's law it follows that $u_e = B_H/(\mu_0 e n l_z) = B_H^2/(3.2 \mu_0 n m_e v_\perp)$. With $\partial u_{ex}/\partial x = u_e/l_u$, and following Refs.^{21,26} we find

$$\begin{aligned} \frac{\partial p_{eyz}}{\partial z} &\simeq 3.6 \frac{\partial p_{eyz}^{\text{Hesse}}}{\partial z} \simeq \frac{3.6}{3.2} \sqrt{\frac{m_e T_e}{2}} \frac{B_H^2}{\mu_0 m_e v_\perp l_u} \\ &\simeq \frac{9}{16} \frac{B_H^2}{\mu_0 l_u} \simeq 0.804 \frac{\Delta p_{e\parallel\perp}^{\text{max}}}{l_u} \simeq \frac{4}{5} \frac{\Delta p_{e\parallel\perp}^{\text{max}}}{l_u}. \end{aligned} \quad (14)$$

As illustrated by the black contours in Figs. 1(c), for the present configurations the momentum balance in Eq. (4) corresponds to the condition $0.7 B_H^2/\mu_0 \simeq \Delta p_{e\parallel\perp}^{\text{max}}$. This substitution was applied in the last line of Eq. (14). Below we will show how the scale factor of 3.6 in front of $\partial p_{eyz}^{\text{Hesse}}/\partial z$ is supported by the numerical data obtained at $m_i/m_e = 1836$, $\beta_{e\infty} \leq 2^{-4}$ (see Fig. 11(a)), and its theoretical origin will be the subject of further investigations.

D. The term breaking the electron frozen in law

Given the described cancellation of terms, the theory suggests that the electron dynamics of the EDR do not represent a bottleneck for reconnection. Again, inserting Eqs. (12) and (13) into Eq. (9) only one term remains for balancing the reconnection electric field

$$E_{\text{rec}} \simeq -\frac{1}{en l_u} \Delta p_{eyy,E}. \quad (15)$$

Separate from the force balance constraint expressed in Eq. (15) we can obtain a second independent estimate for $\Delta p_{eyy,E}$: In Fig. 8 we observe that electrons in the X-line region typically travel a distance between 0 and $2l_u$ in the y -direction such that $\Delta p_{eyy,E} \simeq -en l_u E_{\text{rec}}$. Applying this in Eq. (15) we obtain the seemingly mundane expression that

$$E_{\text{rec}} \simeq E_{\text{rec}}. \quad (16)$$

Nevertheless, this is an important result, as it shows that the present geometry can accommodate any reconnection rate imposed at larger scales onto the EDR region. This is consistent with the near-uniform “ion-normalized-reconnection” rate, α , in Fig. 2(a). It also confirms previous numerical results and theoretical conjectures that, with the formation of electron scale current layers, the electron dynamics can readily accommodate the rates of reconnection imposed by the plasma behavior at larger scales^{7,28,30}. We also note that because $E_{\text{rec}} \propto \Delta p_{eyy,E}/l_u$ and $\Delta p_{eyy,E} \propto l_u$, the reconnection rate becomes independent of l_u . In Appendix C we include additional discussion of how our interpretation of Eqs. (15) and (16) are not in conflict with results of resistive fluid models.

E. Numerical evidence for the validity of the model

As described above, the theory is aided by fully kinetic VPIC simulations carried out for a matrix of $\beta_{e\infty}$ and m_i/m_e values. We next validate each of the separate theoretical predictions against the numerical results. First, the described dynamics involving trapped electrons require that within the inflow regions $|u_{e\parallel}| \ll v_{te}$, which is valid for $\beta_{e\infty} \gtrsim \sqrt{m_e/m_i}^{20,61}$, and the predicted profiles B_H are confirmed in Figs. 10(a).

For all the numerical runs in our study, the individual contributions of $\partial p_{exy}/\partial x$ and $\partial p_{eyz}/\partial z$ are shown in Figs. 10(d,e), respectively. In Fig. 10, E_{rec} is normalized by $T_e/(ed_{e0}) = 0.024$, and for direct comparison, all terms involving pressure derivatives are normalized by $-n_{e\infty} T_{e\infty}/d_{e0}$. With this normalization, confirming Eq. (9), the sum of $\partial p_{exy}/\partial x + \partial p_{eyz}/\partial z$ in Fig. 10(f) reproduces with good accuracy E_{rec} in Fig. 10(c).

Eqs. (10)-(12) represent a key insight for the theory which is confirmed numerically, as Fig. 10(g) provides an accurate representation of Fig. 10(d). Consistent with recent spacecraft observations¹³, $\partial p_{exy}/\partial x$ is mostly negative for runs with $m_i/m_e \geq 400$, and is thus dominated by the external stress imposed by $p_{e\parallel}^{\text{edge}} \gg p_{e\perp}^{\text{edge}}$. Likewise, Eq. (13) is supported by the

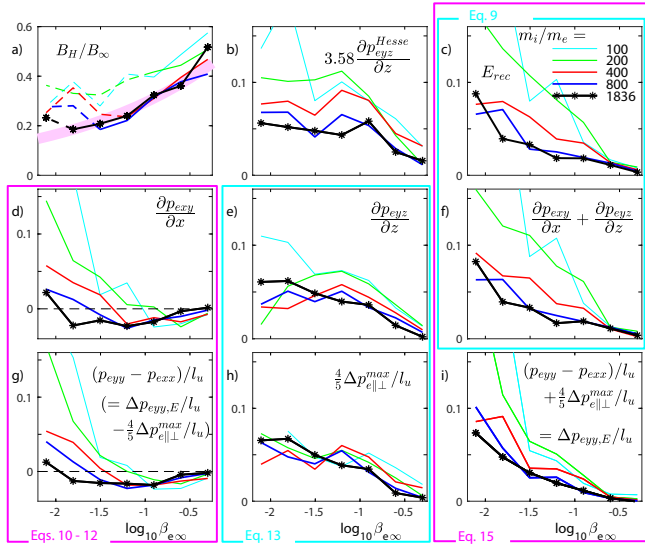


FIG. 10. Obtained from a matrix of 35 kinetic simulations, profiles as functions of $\log_{10}(\beta_{\infty})$ are shown for a range of parameters as marked in the panels. In a) the magenta line is Eq. (4). In c) E_{rec} is normalized by $T_{\infty}/(ed_0)$ (which is different from \hat{E}_{rec} in Fig. 2(b)). The profiles in b), d-i) are various electron pressure tensor derivatives, normalized by $-n_{\times} T_{\infty}/(ed_0)$, such that the resulting dimensionless values can be compared directly to those of E_{rec} in c).

data, as the profiles of $\frac{4}{5} \Delta p_{e\parallel}^{max}/l_u$ in Fig. 10(h), are observed to provide a match to $\partial p_{eyz}/\partial z$ in Fig. 10(e). This is especially the case for $m_i/m_e \geq 400$, corresponding to the adiabatic limit required for the validity of Eq. (4). Also in this limit, the sums shown in Fig. 10(i) of the profiles of Figs. 10(g,h) provide a good match to E_{rec} in Fig. 10(c), confirming Eq. (15).

To further validate the most important equations in the study, in Fig. 11 we plot the terms of Eqs. (9), (11), (13), (14), and (15), with all the shown quantities normalized by $0.1en_{\times}v_A B_{up}$. First, in panel a) the factor of ~ 3.6 used in Eq. (14) is consistent with the data at $m_i/m_e = 1836$, $\beta_{\infty} \leq 2^{-4}$. In panels b) and c) the approximations introduced for $\partial p_{exy}/\partial x$ and $\partial p_{eyz}/\partial z$ are validated. For the case of $\partial p_{eyz}/\partial z$ panel f) indicates an improved accuracy of the approximation for the most relevant parameters of $m_i/m_e \geq 400$ and $\beta_{\infty} \leq 2^{-3}$. From panel d) it is clear that the momentum balance Eq. (9) is well satisfied by the simulations. Panel e) tests the penultimate expression (Eq. (15)) of the paper. Because of the often opposing signs of the $\partial p_{exy}/\partial x$ and $\partial p_{eyz}/\partial z$ estimates, when calculating their sum the relative uncertainty/error is enhanced, explaining the enhanced scatter of the data points. However, as shown in panel g), when limiting the simulations to those with $m_i/m_e \geq 400$ and $\beta_{\infty} \leq 2^{-3}$ most predictions for E_{rec} fall within 20% of the correct value and all predictions are within 50%.

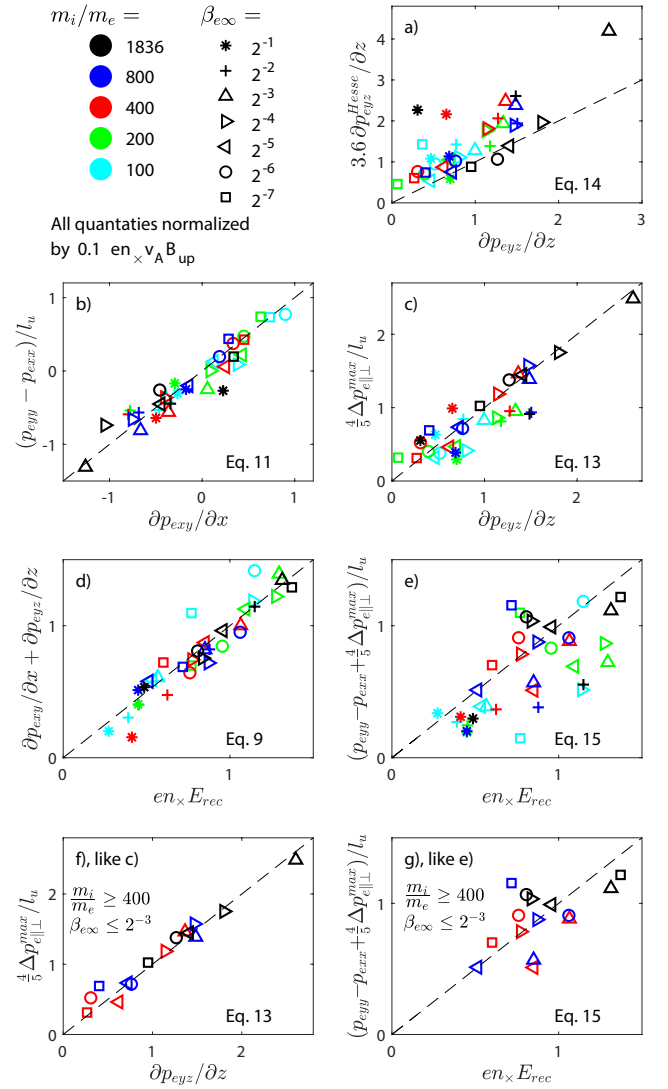


FIG. 11. As indicated in the panels of a-g), the LHS and RHS of key equations of the manuscript are tested using data collected in the numerical runs. Most significantly, in b) Eq. (11) is confirmed, and in f) Eq. (13) is confirmed for the important parameter range of $m_i/m_e \geq 400$ and $\beta_{\infty} \leq 2^{-3}$. To ensure that data from the runs with the largest values of β_{∞} do not cluster close to (0,0), all terms are normalized by $0.1en_{\times}v_A B_{up}$.

VI. SUMMARY AND DISCUSSION

The use of the VPIC code implemented in a modern supercomputing facility enabled a matrix of simulations to be performed for anti-parallel magnetic reconnection. This matrix spans a range of the normalized electron pressures, β_{∞} , as well as the ion to electron mass ratios, m_i/m_e . Our study reveals a range of results, which require new interpretations of the electron dynamics of the EDR and inner IDR that are different from previous models including those in Refs.²¹⁻²³. A main difference from the numerical studies a decade or more ago is our recent ability to carry out routine kinetic simulations at the natural proton to electron mass ratio of

$m_i/m_e = 1836$. At full mass ratio the effect of the electron pressure anisotropy that develops in the reconnection inflow becomes the dominant force-term not only within the EDR but also for the inner part of the IDR.

It has previously been determined^{32,34} that upstream of the EDR strong electron pressure anisotropy with $p_{e\parallel} \gg p_{e\perp}$ is driven by the convection of electrons into the reconnection region characterized by low values of B . This upstream pressure anisotropy is responsible for driving the strong electron currents within the EDR. In addition, with Fig. 3 we visualize how the electron inflow speed for locations inside the IDR (but outside the traditional EDR) exceeds the inflow speed of the magnetic field by a factor up to 3.5. This enhances the Hall magnetic field perturbation beyond what can be expected from traditional “whistler reconnection”²³. Nevertheless, it is still possible that the condition $(\mathbf{J} \times \mathbf{B})_y \simeq (\nabla \cdot \mathbf{p}_e)_y$ is compatible with dispersive waves^{62,63}. The strong Hall field B_y perturbations at the edge of the EDR are mainly a consequence of dynamics related to the electron pressure anisotropy yielding a new and dominate force balance constraint, namely $(\mathbf{J} \times \mathbf{B})_y \simeq (\nabla \cdot \mathbf{p}_e)_y \gg en_e E_{\text{rec}}$. Furthermore, the enhanced perpendicular flow into the EDR by $\mathbf{J}_{\text{extra}} = [(p_{e\parallel} - p_{e\perp})/B]\mathbf{b} \times \boldsymbol{\kappa}$ must be sourced by electrons flowing along the field lines on the inflow-side of the separatrix layers. This is consistent with spacecraft observations that the Hall currents extend many tens of d_i away from the EDR⁶⁴.

Aside from the results summarized above, the main goal of this paper is to develop a theory that can account for the electron momentum balance directly at the X -line within the center of the EDR for anti-parallel reconnection. Previously, Refs.^{21,26} provided approximate expressions for the off-diagonal stress terms $\partial p_{exy}/\partial x$ and $\partial p_{eyz}/\partial z$. After applying a scale factor, their theoretical form for $\partial p_{eyz}/\partial z$ is in agreement with our numerical results. Meanwhile, the electron pressure anisotropy that develops upstream of the EDR turns out to have a large impact on $\partial p_{exy}/\partial x$ not previously considered. Our updated theory for $\partial p_{exy}/\partial x$ is cast in two separate terms. The first term is caused by the upstream electron pressure anisotropy and cancels the stress of $\partial p_{eyz}/\partial z$. In hindsight, this cancellation is not surprising as the EDR current, mainly driven by the upstream $p_{e\parallel} \gg p_{e\perp}$, must be in force balance independent of the value of E_{rec} .

The additional second term for $\partial p_{exy}/\partial x$ in Eq. (12) is the term that scales with E_{rec} and as such, can be considered the term that actually breaks the electron frozen-in condition at the X -line. This term is related to the increase of the p_{eyy} pressure tensor element caused directly through heating by E_{rec} . Because the electron flow in the y -direction is largely fixed by the upstream $p_{e\parallel} \gg p_{e\perp}$ (see Eq. (4)), the increase in p_{eyy} becomes linear in E_{rec} , and the rotation with length scale l_u of p_{eyy} in the xy -plane then yields the stress required to balance E_{rec} . Because the term is proportional to E_{rec} , it facilitates reconnection at any external rate imposed onto the EDR. From the perspective of the electrons the reconnection rate is \hat{E}_{rec} shown in Fig. 10(c), and runs with low values of m_i/m_e have significant enhanced values of \hat{E}_{rec} . Even so, the identified reconnection mechanism can still accommodate these artificially enhanced values of \hat{E}_{rec} .

In closing, we note that our new theory predicts that $\partial p_{exy}/\partial x$ and $\partial p_{eyz}/\partial z$ have opposite signs for $m_i/m_e = 1836$. This result has been directly confirmed in spacecraft observations of an EDR encounter by MMS in the Earth’s magnetotail¹³. Other MMS observations also support the approximation that reconnection in the Earth’s magnetotail occurs in regimes consistent with laminar 2D kinetic models. One reason for the apparent success of such laminar 2D models is perhaps that for $m_i/m_e = 1836$ the force by E_{rec} is small compared to the forces associated with electron pressure anisotropy, such that E_{rec} only slightly perturbs the electron orbit dynamics within the EDR. Again, from the perspective of the electrons the reconnection rates imposed by the inertia and dynamics of the much heavier ions are in fact very modest and the small modifications imposed by E_{rec} on the electron motion is not sufficient to drive strong instabilities. In order for instabilities to alter the momentum equation in Eq. (1) they much have an inverse growth rate similar to the short electron transit time through the EDR. For example, the Lower-Hybrid-Drift-Instability (LHDI) may perturb the out-of-plane structure of the EDR, but this does not necessarily cause a fundamental change in its underlying 2D dynamics^{14,15,65}. Given recent progress in the understanding of how the larger scale ion dynamics influence the reconnection rate^{28,30}, a more detailed and complete picture for reconnection now emerges consistent with local observations of reconnection within the Earth’s magnetotail.

DATA AVAILABILITY

The data that support the findings of this study are available from the corresponding author upon reasonable request. In addition, using the initial conditions specified in the text, the data can be reproduced with the open source VPIC code available online (<https://github.com/lanl/vpic>) (<https://zenodo.org/record/4041845#.X2kA1x17kuY>; <https://doi.org/10.5281/zenodo.4041845>).

APPENDIX A: BASIC MECHANISMS GOVERNING THE FORMATION OF ELECTRON PRESSURE ANISOTROPY UPSTREAM OF THE EDR

As described in Sec. II for anti-parallel reconnection strong electron pressure anisotropy with $p_{e\parallel} \gg p_{e\perp}$ develops within the inflow regions. While this has been the topic of previous investigations^{32,34,66}, for the convenience of the reader we will here provide a short description of the physical mechanisms that governs the generation of the anisotropy. Within the inflow regions the electrons follow the magnetic flux-tubes in their convection toward the EDR, while the ions are unmagnetized. By their inertia, the ions decouple from the motion of the magnetic field, and they dictate a near-uniform plasma density within the region. In turn, the electrons respond strongly to match this uniform density and maintain quasi-neutrality. As illustrated in Fig. 1(a), the declining magnetic field strength $|\mathbf{B}|$ causes the widths of the magnetic flux-

tubes to expand as the EDR is approached. To avoid a reduction in the electron density, field-aligned electric fields E_{\parallel} develop³⁷, compressing the range of the parallel motion for trapped electrons. This boosts the electron density such that quasi-neutrality (i.e. $n_e \simeq n_i$) is maintained. The profiles of E_{\parallel} in many cases trap all thermal electrons, limiting thermal heat conduction and yielding a regime that differs significantly from the standard Boltzmann regime where T_e is constant.

For the trapped electron population, we note that the area of a given flux-tube scales as $1/B$, and the total number of trapped particles in the flux-tube section (of length l) therefore scales as $N_{\text{trapped}} \propto n_{\text{trapped}} l/B$. For the case where the trapped electrons dominate the full distribution, particle conservation then requires that $l \propto B/n_{\text{trapped}}$. Next, similar to Fermi heating, the conservation of the parallel action for each trapped electron requires that $l v_{\parallel}$ is constant such that $v_{\parallel} \propto n_{\text{trapped}}/B$, yielding $T_{e\parallel} \propto v_{\parallel}^2 \propto n_{\text{trapped}}^2/B^2$. Furthermore, because $\mu = m v_{\perp}^2/(2B)$ is conserved it is clear that $v_{\perp}^2 \propto B$, such that for this trapped electron population $T_{e\perp} \propto B$. It then follows that $p_{e\parallel} = n T_{e\parallel} \propto n_{\text{trapped}}^3/B^2$ and $p_{e\perp} = n T_{e\perp} \propto n_{\text{trapped}} B$, coinciding with the CGL-scaling laws³⁵. Again, more accurate scaling laws are provided in Refs.^{32,34}, taking into account that not all electrons become trapped. This yields a smooth transition from Boltzmann scaling ($p_{e\parallel} = p_{e\perp} = n T_e$) at low values of n/B to the CGL scalings at large values of n/B .

APPENDIX B: FORCE BALANCE ALONG THE EDR

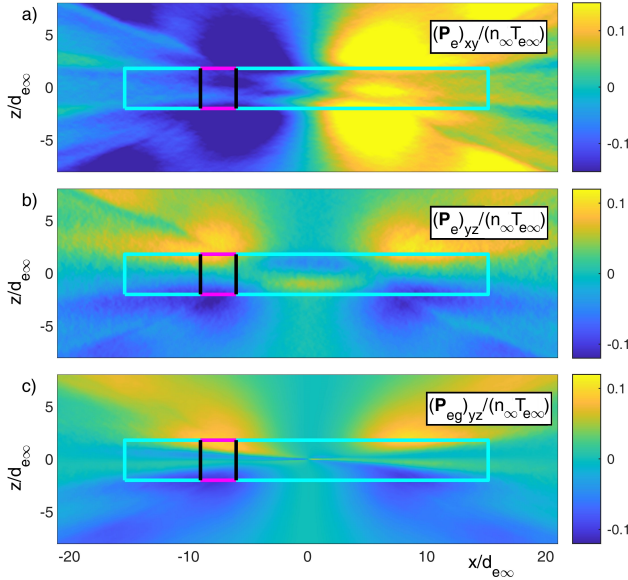


FIG. 12. Considering the same simulation ($m_i/m_e = 1836$ and $\beta_{e\infty} = 2^{-4}$) as in Fig. 1, color contours are presented for a) $p_{e,xy}$, b) $p_{e,yz}$, and c) $p_{eg,yz}$. The EDR is outlined by the cyan rectangle, and a fluid-element is selected for analysis by the black/magenta square.

When away from the vicinity of the X -line, the $\mathbf{J} \times \mathbf{B}$ -forces within the EDR are large (see Fig. 3(a)), and in Fig. 12 we

explore how the large values of $(\mathbf{J} \times \mathbf{B})_y$ are related to the electron pressure anisotropy that forms upstream of the EDR. For this, consider the small fluid element which in each panel is marked by the black/magenta square. Naturally, we can integrate Eq. (6) over the surface of this fluid element. For the RHS of Eq. (6) the largest contribution is from $\int (\nabla \cdot \mathbf{p}_e)_y dA$. In turn, by the divergence theorem $\int (\nabla \cdot \mathbf{p}_e)_y dA = \Delta p_{exy} \Delta z + \Delta p_{eyz} \Delta x$. Here, Δp_{exy} is the change in p_{exy} between the two black sides of the element, while Δp_{eyz} is the change in p_{eyz} between the two magenta sides. Comparing Figs. 12(a,b) it is clear that $|\Delta p_{exy}| \ll |\Delta p_{eyz}|$, such that $\int (\nabla \cdot \mathbf{p}_e)_y dA \simeq \Delta p_{eyz} \Delta x$.

We have now demonstrated that $\int (\mathbf{J} \times \mathbf{B})_y dA \simeq \Delta p_{eyz} \Delta x$. On the other hand, $\mathbf{J} \times \mathbf{B} = \nabla \cdot \mathbf{T}$, where $\mathbf{T} = (B^2/\mu_0)(\mathbf{bb} - \mathbf{I}/2)$ is the Maxwell stress tensor. By similar arguments to those applied when integrating $\int (\nabla \cdot \mathbf{p}_e)_y dA$, we then find that $\int (\mathbf{J} \times \mathbf{B})_y dA = \int (\nabla \cdot \mathbf{T})_y dA \simeq \Delta T_{yz} \Delta x$. Note that for the fluid element with $\Delta x \simeq \Delta z$, we have $\Delta T_{yz} \Delta x \gg \Delta T_{xy} \Delta z$ due to the $\simeq 1/10$ aspect ratio of the full EDR. Neglecting E_y , the force balance constraint in Eq. (5) can then be expressed as $\Delta T_{yz} \simeq \Delta p_{eyz}$, and given these elements are asymmetric about $z = 0$ this further reduces to $T_{yz} \simeq p_{eyz}$ along the upstream edge of the EDR. An identical analysis can be carried out for the forces in the x -direction, which yields the similar result that $T_{xz} \simeq p_{exz}$ along the upstream edge of the EDR.

The integrals over the fluid element involved the full pressure tensor \mathbf{p}_e , but by the divergence theorem the results only depend on the values of \mathbf{p}_e at the upstream edge of the EDR; here \mathbf{p}_e is well approximated by its CGL-form $\mathbf{p}_e \simeq p_{eg} = (p_{e\parallel} - p_{e\perp})\mathbf{bb} + p_{e\perp}\mathbf{I}$. To illustrate that $\mathbf{p}_e \simeq p_{eg}$ outside the EDR, in Figs. 12(b,c) the profiles of p_{eyz} and $p_{eg,yz}$ can be compared directly. Simple manipulations then show that the two force balance constraints that $T_{yz} \simeq p_{eyz}$ and $T_{xz} \simeq p_{exz}$, can now be expressed on a common form through the marginal firehose condition $p_{e\parallel} - p_{e\perp} = B^2/\mu_0$, again, applicable along the upstream edge of the EDR.

To summarize this analysis, we have shown that for the present simulation at $m_i/m_e = 1836$ that $|en_e E_y| \ll |(\mathbf{J} \times \mathbf{B})_y| \simeq |(\nabla \cdot \mathbf{p}_e)_y|$. By integrating over a fluid element that spans the width of the EDR, it is then found that the strong $\mathbf{J} \times \mathbf{B}$ -forces within the EDR are balanced by the force of the pressure anisotropy at the upstream edge of the EDR. In turn, at the upstream edge of the EDR the L  2009 equations of state³⁴ are applicable, and together with the force balance condition $p_{e\parallel} - p_{e\perp} = B^2/\mu_0$, this leads to the scaling law for the current across the EDR as expressed in Eq. (4). It is noteworthy here how the current across the EDR is expressed in terms of parameters evaluated far upstream of the reconnection region.

APPENDIX C: CONNECTION TO RESULTS OF RESISTIVE-MHD

A critical reader may argue that the result in Eq. (15) was just obtained two different ways, and the statement in Eq. (16) therefore becomes trivial. However, here it should be noted that Eq. (15) was obtained based momentum balance constraints, while $\Delta p_{eyy,E} \simeq -en_l u E_{\text{rec}}$ applied to the RHS of

Eq. (15) represents the separate issues related to electron heating. As such, Eq. (16) can be considered a meaningful mathematical expression describing the independence of E_{rec} from the EDR dynamics, valid for any E_{rec} sufficiently small that it does not alter the basic dynamics that lead to Eq. (15).

We also note that our interpretation of Eqs. (15) and (16) is not in conflict with results from resistive fluid models. For the particular case of an MHD plasma with resistivity η , the reconnection electric field is $E_{\text{rec}} = \eta J$, and the heating rate, $\mathbf{E} \cdot \mathbf{J}$, scales proportionally to E_{rec}^2 . Power-balance arguments can then be invoked to quantify the much slower rate of reconnection characteristic of resistive MHD^{54,67}. In such fluid models with an imposed isotropic pressure, it is (by definition) not possible for E_{rec} to change p_{eyy} without introducing identical changes in p_{exx} (and p_{ezz}). Therefore, Eq. (15) is then not applicable and the analysis applied in resistive MHD has no implications on the collisionless anti-parallel case studied here. In fact, as shown in Ref.⁴⁵, when the energy continuity equation is applied to the collisionless EDR of anti-parallel reconnection, we obtain a prediction of the net electron heating level across the EDR, which does not impose a constraint on E_{rec} .

For the related case of collisionless guide-field reconnection, the structure of the EDR is qualitatively different as it does not include the jets of meandering electrons³⁴. Further investigations are therefore needed to determine if the present framework can be generalized to scenarios including an out-of-plane guide magnetic field.

APPENDIX D: CHARACTERISTIC LENGTH SCALES OF THE SIMULATION DOMAINS

TABLE I. Parameters describing the numerical simulation sizes in the x -direction. In the z -direction the domains all have half the size of the x -direction. For example, for $m_i/m_e = 1836$ the domains are characterized by $L_x/d_{ep} \times L_z/d_{ep} = 1000 \times 500$.

Table I.A: L_x/d_{ep} , L_x/d_{ip} , # of x -cells					
$m_i/m_e = 100$	200	400	800	1836	
L_x/d_{ep}	500	707	1000	1000	1000
L_x/d_{ip}	50	50	50	35.35	23.34
# of x -cells	3960	3960	5632	5632	5632

Table I.B: $L_x/d_{e\infty}$					
$m_i/m_e = 100$	200	400	800	1836	
$\beta_{e\infty} = 2^{-1}$	433	612	866	866	866
2^{-2}	387	548	775	775	775
2^{-3}	327	463	655	655	655
2^{-4}	261	369	522	522	522
2^{-5}	199	281	397	397	397
2^{-6}	146	207	293	293	293
2^{-7}	106	150	212	212	212

Table I.C: $L_x/d_{i\infty}$					
$m_i/m_e = 100$	200	400	800	1836	
$\beta_{e\infty} = 2^{-1}$	43.3	43.3	43.3	30.6	20.2
2^{-2}	38.7	38.7	38.7	27.4	18.1
2^{-3}	32.7	32.7	32.7	23.1	15.3
2^{-4}	26.1	26.1	26.1	18.5	12.2
2^{-5}	19.9	19.9	19.9	14.0	9.3
2^{-6}	14.6	14.6	14.6	10.4	6.8
2^{-7}	10.6	10.6	10.6	7.5	4.9

- ¹J. Dungey, "Conditions for the occurrence of electrical discharges in astrophysical systems," *Philosophical Magazine* **44**, 725 (1953).
- ²S. Masuda, T. Kosugi, H. Hara, and Y. Ogawaray, "A loop top hard x-ray source in a compact solar-flare as evidence for magnetic reconnection," *Nature* **371**, 495–497 (1994).
- ³R. McPherron, C. Russell, and M. Aubry, "Satellite studies of magnetospheric substorms on August 15, 1968. 9. phenomenological model for substorms," *J. Geophys. Res.* **78**, 3131–3149 (1973).
- ⁴E. N. Parker, "Sweet's mechanism for merging magnetic fields in conducting fluids," *J. Geophys. Res.* **62**, 509 (1957).
- ⁵J. Birn, J. F. Drake, M. A. Shay, B. N. Rogers, R. E. Denton, M. Hesse, M. Kuznetsova, Z. W. Ma, A. Bhattacharjee, A. Otto, and P. L. Pritchett, "Geospace environmental modeling (GEM) magnetic reconnection challenge," *J. Geophys. Res.* **106**, 3715–3719 (2001).
- ⁶O. Ohia, J. Egedal, V. S. Lukin, W. Daughton, and A. Le, "Demonstration of Anisotropic Fluid Closure Capturing the Kinetic Structure of Magnetic Reconnection," *Phys. Rev. Lett.* **109** (2012), 10.1103/PhysRevLett.109.115004.
- ⁷M. A. Shay, J. F. Drake, B. N. Rogers, and R. E. Denton, "The scaling of collisionless, magnetic reconnection for large systems," *Geophys. Res. Lett.* **26**, 2163–2166 (1999).
- ⁸E. G. Zweibel and M. Yamada, "Perspectives on magnetic reconnection," *Proc. R. Soc. A* **472** (2016), 10.1098/rspa.2016.0479.
- ⁹I. Silin, J. Büchner, and A. Vaivads, "Anomalous resistivity due to non-linear lower-hybrid drift waves," *Physics of Plasmas* **12**, 062902 (2005), <https://doi.org/10.1063/1.1927096>.
- ¹⁰H. Che, J. F. Drake, and M. Swisdak, "A current filamentation mechanism for breaking magnetic field lines during reconnection," *Nature* **474**, 184–187 (2011).
- ¹¹P. A. Muñoz, J. Büchner, and P. Kilian, "Turbulent transport in 2d collisionless guide field reconnection," *Physics of Plasmas* **24**, 022104 (2017), <https://doi.org/10.1063/1.4975086>.
- ¹²J. Egedal, A. Le, W. Daughton, B. Wetherington, P. A. Cassak, J. L. Burch, B. Lavraud, J. Dorelli, D. J. Gershman, and L. A. Avanov, "Spacecraft Observations of Oblique Electron Beams Breaking the Frozen-In Law During Asymmetric Reconnection," *Phys. Rev. Lett.* **120** (2018), 10.1103/PhysRevLett.120.055101.
- ¹³J. Egedal, J. Ng, A. Le, W. Daughton, B. Wetherington, J. Dorelli, D. Gershman, and A. Rager, "Pressure tensor elements breaking the frozen-in law during reconnection in earth's magnetotail," *Phys. Rev. Lett.* **123**, 225101 (2019).
- ¹⁴S. Greess, J. Egedal, A. Stanier, W. Daughton, J. Olson, A. Le, R. Myers, A. Millet-Ayala, M. Clark, J. Wallace, D. Endrizzi, and C. Forest, "Laboratory verification of electron-scale reconnection regions modulated by a three-dimensional instability," *J. Geophys. Res.* **126** (2021), 10.1029/2021JA029316.
- ¹⁵J. M. Schroeder, J. Egedal, G. Cozzani, Y. V. Khotyaintsev, W. Daughton, R. E. Denton, and J. L. Burch, "2D Reconstruction of Magnetotail Electron Diffusion Region Measured by MMS," *Geophys. Res. Lett.* **49**, e2022GL100384 (2022), e2022GL100384 2022GL100384, <https://agupubs.onlinelibrary.wiley.com/doi/pdf/10.1029/2022GL100384>.
- ¹⁶R. B. Torbert, J. L. Burch, T. D. Phan, M. Hesse, M. R. Argall, J. Shuster, R. E. Ergun, L. Alm, R. Nakamura, K. J. Genestreti, D. J. Gershman, W. R. Paterson, D. L. Turner, I. Cohen, B. L. Giles, C. J. Pollock, S. Wang, L.-J. Chen, J. E. Stawarz, J. P. Eastwood, K. J. Hwang, C. Farrugia, I. Dors, H. Vaith, C. Mouikis, A. Ardakani, B. H. Mauk, S. A. Fuselier, C. T. Russell, R. J. Strangeway, T. E. Moore, J. F. Drake, M. A. Shay, Y. V. Khotyaintsev, P.-A. Lindqvist, W. Baumjohann, F. D. Wilder, N. Ahmadi, J. C. Dorelli, L. A. Avanov, M. Oka, D. N. Baker, J. F. Fennell, J. B. Blake, A. N. Jaynes, O. Le Contel, S. M. Petrinec, B. Lavraud, and Y. Saito, "Electron-scale dynamics of the diffusion region during symmetric magnetic reconnection in space," *Science* (2018), 10.1126/science.aat2998, <http://science.sciencemag.org/content/early/2018/11/14/science.aat2998.full.pdf>.
- ¹⁷X. Ma, K. Nykyri, A. Dimmock, and C. Chu, "Statistical study of solar wind, magnetosheath, and magnetotail plasma and field properties: 12+ years of THEMIS observations and MHD simulations," *Journal of Geophysical Research: Space Physics* **125**, e2020JA028209 (2020), e2020JA028209 10.1029/2020JA028209, <https://agupubs.onlinelibrary.wiley.com/doi/pdf/10.1029/2020JA028209>.
- ¹⁸A. Le, J. Egedal, O. Ohia, W. Daughton, H. Karimabadi, and V. S. Lukin, "Regimes of the Electron Diffusion Region in Magnetic Reconnection," *Phys. Rev. Lett.* **110** (2013), 10.1103/PhysRevLett.110.135004.
- ¹⁹J. Egedal, W. Daughton, and A. Le, "Large-scale electron acceleration by parallel electric fields during magnetic reconnection," *Nature Physics* **8**, 321–324 (2012).
- ²⁰J. Egedal, W. Daughton, A. Le, and A. L. Borg, "Double layer electric fields aiding the production of energetic flat-top distributions and superthermal electrons within magnetic reconnection exhausts," *Phys. Plasmas* **22** (2015), 10.1063/1.4933055.
- ²¹M. Hesse, K. Schindler, J. Birn, and M. Kuznetsova, "The diffusion region in collisionless magnetic reconnection," *Phys. Plasmas* **6**, 1781–1795 (1999), 40th Annual Meeting of the Division of Plasma Physics of the American-Physical-Society, New Orleans, Louisiana, Nov 16-20, 1998.
- ²²W. Daughton, J. Scudder, and K. Homa, "Fully kinetic simulations of undriven magnetic reconnection with open boundary conditions," *Phys. Plasmas* **13**, 072101 (2006).
- ²³J. F. Drake, M. A. Shay, and M. Swisdak, "The Hall fields and fast magnetic reconnection," *Phys. Plasmas* **15** (2008), 10.1063/1.2901194.
- ²⁴M. A. Shay, J. F. Drake, and M. Swisdak, "Two-scale structure of the electron dissipation region during collisionless magnetic reconnection," *Phys. Rev. Lett.* **99** (2007), 10.1103/PhysRevLett.99.155002.
- ²⁵H. Karimabadi, W. Daughton, and J. Scudder, "Multi-scale structure of the electron diffusion region," *Geophys. Res. Lett.* **34** (2007), 10.1029/2007GL030306.
- ²⁶M. M. Kuznetsova, M. Hesse, and D. Winske, "Kinetic quasi-viscous and bulk flow inertia effects in collisionless magnetotail reconnection," *J. Geophys. Res.* **103**, 199–213 (1998).
- ²⁷P. A. Cassak, Y. H. Liu, and M. A. Shay, "A review of the 0.1 reconnection rate problem," *Journal of Plasma Physics* **83** (2017), 10.1017/S0022377817000666.
- ²⁸Y.-H. Liu, M. Hesse, F. Guo, W. Daughton, H. Li, P. A. Cassak, and M. A. Shay, "Why does steady-state magnetic reconnection have a maximum local rate of order 0.1?" *Phys. Rev. Lett.* **118**, 085101 (2017).
- ²⁹A. Le, J. Egedal, J. Ng, H. Karimabadi, J. Scudder, V. Roytershteyn, W. Daughton, and Y. H. Liu, "Current sheets and pressure anisotropy in the reconnection exhaust," *Phys. Plasmas* **21** (2014), 10.1063/1.4861871.
- ³⁰A. Stanier, W. Daughton, L. Chacon, H. Karimabadi, J. Ng, Y. M. Huang, A. Hakim, and A. Bhattacharjee, "Role of ion kinetic physics in the interaction of magnetic flux ropes," *Phys. Rev. Lett.* **115** (2015), 10.1103/PhysRevLett.115.175004.
- ³¹A. Le, J. Egedal, W. Daughton, J. F. Drake, W. Fox, and N. Katz, "Magnitude of the hall fields during magnetic reconnection," *Geophysical Research Letters* **37** (2010), <https://doi.org/10.1029/2009GL041941>, <https://agupubs.onlinelibrary.wiley.com/doi/pdf/10.1029/2009GL041941>.
- ³²J. Egedal, A. Le, and W. Daughton, "A review of pressure anisotropy caused by electron trapping in collisionless plasma, and its implications for magnetic reconnection," *Phys. Plasmas* **20** (2013), 10.1063/1.4811092.
- ³³P. Montag, J. Egedal, and W. Daughton, "Influence of Inflow Density and Temperature Asymmetry on the Formation of Electron Jets during Magnetic Reconnection," *Geophys. Res. Lett.* **47** (2020), 10.1029/2020GL087612.
- ³⁴A. Le, J. Egedal, W. Daughton, W. Fox, and N. Katz, "Equations of state for collisionless guide-field reconnection," *Phys. Rev. Lett.* **102**, 085001 (2009).
- ³⁵G. F. Chew, M. L. Goldberger, and F. E. Low, "The boltzmann equation and the one-fluid hydromagnetic equations in the absence of particle collisions," *Proc. Royal Soc. A* **112**, 236 (1956).
- ³⁶J. Egedal, B. Wetherington, W. Daughton, and A. Le, "Processes setting the structure of the electron distribution function within the exhausts of anti-parallel reconnection," *Phys. Plasmas* **23** (2016), 10.1063/1.4972135.
- ³⁷J. Egedal, W. Daughton, J. F. Drake, N. Katz, and A. Le, "Formation of a localized acceleration potential during magnetic reconnection with a guide field," *Phys. Plasmas* **16** (2009), 10.1063/1.3130732.
- ³⁸H. Gurram, J. Egedal, and W. Daughton, "Shear alfvén waves driven by magnetic reconnection as an energy source for the aurora borealis," *Geophys. Res. Lett.* **48** (2021), 10.1029/2021GL094201.
- ³⁹A. Le, J. Egedal, W. Fox, N. Katz, A. Vrublevskis, W. Daughton, and J. F. Drake, "Equations of state in collisionless magnetic reconnection," *Phys. Plasmas* **17**, 055703 (2010), 51st Annual Meeting of the Division of Plasma Physics of the American Physical Society, Atlanta, GA, NOV 02-06, 2009.

- ⁴⁰R. Horiuchi and T. Sato, "Particle simulation study of collisionless driven reconnection in a sheared magnetic field," *Phys. Plasmas* **4**, 277–289 (1997).
- ⁴¹M. Shay and J. Drake, "The role of electron dissipation on the rate of collisionless magnetic reconnection," *Geophys. Res. Lett.* **25**, 3759–3762 (1998).
- ⁴²V. Roytershteyn, S. Dorfman, W. Daughton, H. Ji, M. Yamada, and H. Karimabadi, "Electromagnetic instability of thin reconnection layers: Comparison of three-dimensional simulations with MRX observations," *Physics of Plasmas* (2013), 10.1063/1.4811371.
- ⁴³M. Mandt, R. Denton, and J. Drake, "Transition to whistler mediated magnetic reconnection," *Geophys. Res. Lett.* **21**, 73–76 (1994).
- ⁴⁴M. Hesse, S. Zenitani, and A. Klimas, "The structure of the electron outflow jet in collisionless magnetic reconnection," *Phys. Plasmas* **15** (2008), 10.1063/1.3006341.
- ⁴⁵A. Le, J. Egedal, and W. Daughton, "Two-stage bulk electron heating in the diffusion region of anti-parallel symmetric reconnection," *Phys. Plasmas* **23** (2016), 10.1063/1.4964768.
- ⁴⁶K. Bowers, B. Albright, L. Yin, W. Daughton, V. Roytershteyn, B. Bergen, and T. Kwan, "Advances in petascale kinetic plasma simulation with VPIC and Roadrunner," *Journal of Physics: Conference Series* **180**, 012055 (10 pp.) (2009).
- ⁴⁷M. Shay, J. Drake, M. Swisdak, and B. Rogers, "The scaling of embedded collisionless reconnection," *Phys. Plasmas* **11**, 2199–2213 (2004).
- ⁴⁸T. D. Phan, J. P. Eastwood, M. A. Shay, J. F. Drake, B. U. O. Sonnerup, M. Fujimoto, P. A. Cassak, M. Oieroset, J. L. Burch, R. B. Torbert, A. C. Rager, J. C. Dorelli, D. J. Gershman, C. Pollock, P. S. Pyakurel, C. C. Haggerty, Y. Khotyaintsev, B. Lavraud, Y. Saito, M. Oka, R. E. Ergun, A. Retino, O. Le Contel, M. R. Argall, B. L. Giles, T. E. Moore, F. D. Wilder, R. J. Strangeway, C. T. Russell, P. A. Lindqvist, and W. Magnes, "Electron magnetic reconnection without ion coupling in earth's turbulent magnetosheath," *Nature* **557**, 202+ (2018).
- ⁴⁹P. S. Pyakurel, M. A. Shay, T. D. Phan, W. H. Matthaeus, J. F. Drake, J. M. TenBarge, C. C. Haggerty, K. G. Klein, P. A. Cassak, T. N. Parashar, M. Swisdak, and A. Chasapis, "Transition from ion-coupled to electron-only reconnection: Basic physics and implications for plasma turbulence," *Phys. Plasmas* **26** (2019), 10.1063/1.5090403.
- ⁵⁰J. Olson, J. Egedal, M. Clark, D. A. Endrizzi, S. Greess, A. Millet-Ayala, R. Myers, E. E. Peterson, J. Wallace, and C. B. Forest, "Regulation of the normalized rate of driven magnetic reconnection through shocked flux pileup," *Journal of Plasma Physics* **87** (2021), 10.1017/S0022377821000659.
- ⁵¹S. Greess, J. Egedal, A. Stanier, J. Olson, W. Daughton, A. Le, A. Millet-Ayala, C. Kuchta, and C. B. Forest, "Kinetic simulations verifying reconnection rates measured in the laboratory, spanning the ion-coupled to near electron-only regimes," *Phys. Plasmas* **29** (2022), 10.1063/5.0101006.
- ⁵²V. M. Vasyliunas, "Theoretical models of magnetic-field line merging .1," *Reviews of Geophysics* **13**, 303–336 (1975).
- ⁵³H. J. Cai, D. Q. Ding, and L. C. Lee, "Momentum transport near a magnetic x line in collisionless reconnection," *Journal of Geophysical Research: Space Physics* **99**, 35–42 (1994), <https://agupubs.onlinelibrary.wiley.com/doi/pdf/10.1029/93JA02519>.
- ⁵⁴Y.-H. Liu, P. Cassak, X. Li, M. Hesse, S.-C. Lin, and K. Genestreti, "First-principles theory of the rate of magnetic reconnection in magnetospheric and solar plasmas," *COMMUNICATIONS PHYSICS* **5** (2022), 10.1038/s42005-022-00854-x.
- ⁵⁵D. S. Payne, C. J. Farrugia, R. B. Torbert, K. Germaschewski, A. R. Rogers, and M. R. Argall, "Origin and structure of electromagnetic generator regions at the edge of the electron diffusion region," *Phys. Plasmas* **28** (2021), 10.1063/5.0068317.
- ⁵⁶J. L. Burch, J. M. Webster, M. Hesse, K. J. Genestreti, R. E. Denton, T. D. Phan, H. Hasegawa, P. A. Cassak, R. B. Torbert, B. L. Giles, D. J. Gershman, R. E. Ergun, C. T. Russell, R. J. Strangeway, O. Le Contel, K. R. Pritchard, A. T. Marshall, K. J. Hwang, K. Dokgo, S. A. Fuselier, L. J. Chen, S. Wang, M. Swisdak, J. F. Drake, M. R. Argall, K. J. Trattner, M. Yamada, and G. Paschmann, "Electron inflow velocities and reconnection rates at earth's magnetopause and magnetosheath," *Geophys. Res. Lett.* **47** (2020), 10.1029/2020GL089082.
- ⁵⁷J. Ng, J. Egedal, A. Le, W. Daughton, and L. J. Chen, "Kinetic structure of the electron diffusion region in antiparallel magnetic reconnection," *Phys. Rev. Lett.* **106** (2011), 10.1103/PhysRevLett.106.065002.
- ⁵⁸T. Speiser, "Particle trajectories in model current sheets .i. analytical solutions," *J. Geophys. Res.* **70**, 4219 (1965).
- ⁵⁹J. R. Shuster, L. J. Chen, M. Hesse, M. R. Argall, W. Daughton, R. B. Torbert, and N. Bessho, "Spatiotemporal evolution of electron characteristics in the electron diffusion region of magnetic reconnection: Implications for acceleration and heating," *Geophys. Res. Lett.* **42**, 2586–2593 (2015).
- ⁶⁰A. Divin, V. Semenov, D. Korovinskiy, S. Markidis, J. Deca, V. Olshevsky, and G. Lapenta, "A new model for the electron pressure nongyrotropy in the outer electron diffusion region," *Geophys. Res. Lett.* **43**, 10,565–10,573 (2016), <https://agupubs.onlinelibrary.wiley.com/doi/pdf/10.1002/2016GL070763>.
- ⁶¹A. Le, J. Egedal, W. Daughton, V. Roytershteyn, H. Karimabadi, and C. Forest, "Transition in electron physics of magnetic reconnection in weakly collisional plasma," *Journal of Plasma Physics* **81** (2015), 10.1017/S0022377814000907.
- ⁶²B. N. Rogers, R. E. Denton, J. F. Drake, and M. A. Shay, "Role of dispersive waves in collisionless magnetic reconnection," *Phys. Rev. Lett.* **8719**, 195004 (2001).
- ⁶³P. A. Cassak, R. N. Baylor, R. L. Fermo, M. T. Beidler, M. A. Shay, M. Swisdak, J. F. Drake, and H. Karimabadi, "Fast magnetic reconnection due to anisotropic electron pressure," *PHYSICS OF PLASMAS* **22** (2015), 10.1063/1.4908545.
- ⁶⁴M. Manapat, M. Oieroset, T. D. Phan, R. P. Lin, and M. Fujimoto, "Field-aligned electrons at the lobe/plasma sheet boundary in the mid-to-distant magnetotail and their association with reconnection," *Geophysical Research Letters* **33** (2006), <https://doi.org/10.1029/2005GL024971>, <https://agupubs.onlinelibrary.wiley.com/doi/pdf/10.1029/2005GL024971>.
- ⁶⁵A. Le, W. Daughton, L. J. Chen, and J. Egedal, "Enhanced electron mixing and heating in 3-D asymmetric reconnection at the Earth's magnetopause," *Geophys. Res. Lett.* **44**, 2096–2104 (2017).
- ⁶⁶J. Egedal, W. Fox, N. Katz, M. Porkolab, M. Oieroset, R. P. Lin, W. Daughton, and D. J. F., "Evidence and theory for trapped electrons in guide field magnetotail reconnection," *J. Geophys. Res.* **113**, A12207 (2008).
- ⁶⁷W. M. Manheimer and C. Lashmore-Davies, "Mhd (magnetohydrodynamics) instabilities in simple plasma configuration," (1984), <https://www.osti.gov/biblio/6204270>.